Dilatancy and tensile criteria for salt cavern design in the context of cyclic loading for energy storage

P. Labaune, Ahmed Rouabhi

Dilatancy and tensile criteria for salt cavern design in the context of cyclic loading for energy storage

P. Labaune*, A. Rouabhi

MINES ParisTech, PSL Research University, Centre de Géosciences, 35 rue St Honoré 77300 Fontainebleau, France

Abstract

In the current energy transition context, salt caverns are promising for massive energy storage but their design methodology needs to be updated to face the challenge of new operating scenarios. This work proposes a new methodology based on the development of a new rheological model that includes dilatancy and tensile criteria, consistent with the long and short term conditions.

To illustrate the difference between the classical and the new methodologies, fully coupled thermo-mechanical numerical simulations of a spherical cavern, filled with either methane or hydrogen, and the surrounding rock salt are performed under various cycling scenarios. Although the two studied gases show distinctive thermodynamic behaviors, the storage of hydrogen does not raise new issues in terms of the cavern design. Concerning the operation history, in addition to the fact that lowering the cycling amplitude limits the development of dilatancy and tension, it is observed that employing a high cycling rate leaves the dilatancy unchanged but intensifies the tension, both in extent and magnitude, even for a small cycling amplitude.

Keywords: Underground storage; Salt rheology; Multi-mechanism model; Cavern design; Dilatancy criteria; Tensile criteria

*Corresponding author
Email address: paule.labaune@mines-paristech.fr (P. Labaune)

List of main symbols

t	Time (s)
$\underline{\underline{\sigma}}$	Stress tensor (Pa)
p, q, θ	Invariants of the stress tensor (Pa, Pa, rad)
$\underline{\underline{I}}$, $\underline{\underline{J}}$, $\underline{\underline{K}}$	Orthonormal basis of the stress space (-)
$\underline{\underline{N}}^c$, $\underline{\underline{N}}^t$	Deviatoric unit tensors (-)
$\sigma_1 \geq \sigma_2 \geq \sigma_3$	Principal stresses (Pa)
$\varrho(\theta)$	Function defining the deviatoric cross-section (-)
$\underline{\underline{\varepsilon}}$, $\underline{\underline{\varepsilon}}_{vp}$	Total and viscoplastic strain tensors (-)
$\underline{\underline{\varepsilon}}^c_{vp}$, $\underline{\underline{\varepsilon}}^t_{vp}$	Compressive and tensile viscoplastic strain tensors (-)
γ, γ_e, γ_{vp}	Total, elastic and viscoplastic distortion strains (-)
γ^c_{vp}, γ^t_{vp}	Compressive and tensile viscoplastic distortion strains (-)
ζ, ζ_e, ζ_{vp}	Total, elastic and viscoplastic volumetric strains (-)
ζ^c_{vp}, ζ^t_{vp}	Compressive and tensile viscoplastic volumetric strains (-)
λ	Tensile viscoplastic strain (-)
T	Temperature (°C)
P	Cavern pressure (Pa)

1. Introduction

In the energy transition context, the intermittent and often unpredictable nature of renewable energy requires massive storage systems. Salt caverns are one of the most promising techniques, as they are able to deliver high flow rates and are reversible and cost-efficient. Salt caverns have been used for decades to store hydrocarbons, especially natural gas, and are usually operated on an annual basis: gas is injected into the cavern in the summer, when the production exceeds the demand, and withdrawn in the winter, when the demand is higher [1–4]. Their use for new energy storage purposes raises new questions. First, the cycling rate varies drastically: the classical seasonal scenarios are being replaced with much quicker and potentially erratic scenarios (up to daily cycles). Second, new fluids with different thermodynamic behaviors are being stored: for example, natural gas gives way to carbon dioxide or hydrogen (in the case of the PtG [5–8]), or compressed air (in the case of the CAES [9, 10]). Addressing these issues requires a suitable, accurate and reliable design methodology.

The classical approach to design a salt cavern consists of two successive steps: simulation of the cavern with rheological models and then interpretation of the results with design criteria. Many different rheological models of varying complexity and specificity have been developed over the years [11–18]. In turn, design criteria are used in post-processing, to determine the stability and serviceability of salt caverns previously simulated with creep laws. The design criteria consist of setting thresholds on various quantities (non-elastic strain or strain rate, tensile stress, shear stress, etc.), allowing one to define admissible stresses and strains. For example, tensile criteria are based on the maximum principal stress and on a threshold determined experimentally through Brazilian tests. Another example are dilatancy criteria, which define a boundary in the stress space between the contracting and dilating behavior of rock salt and are experimentally defined through short-term triaxial tests [19–23]. Dilatancy and tensile criteria are often used in feasibility studies, either jointly [24–26] or independently [27–32].

However, this classical approach is often faced with excessive conservationism and inconsistencies between creep laws and design criteria. Attention is frequently restricted to the stress state at the cavern wall, where criteria are first and quickly exceeded, which causes several problems. First, the extent of the damage might be limited and the cavern operation still safe. Then, it is reasonable to assume the stress state to be altered by the dilatancy and tensile phenomena, and it does not make sense to study the stress state at the cavern wall long after the criteria are exceeded. Additionally, the fact that these criteria alternate between being satisfied and exceeded over each cycle (see for example [29]) is in contradiction with the idea that dilatancy and tensile zones should not decrease over time, as they are associated with irreversible phenomena. Some rheological models, such as [33], do consider that the healing phenomenon can reduce the damage, but it seems exaggerated to consider that it can totally erase dilatancy or tension between each cycle, especially in the case of high cycling rates. Moreover, creep laws and design criteria are not integrated in a fully consistent and unified methodology. Creep laws are fitted based on long-term creep tests, whereas design criteria are based on short-term tests, and we find ourselves with two disconnected models juxtaposed without further justification. Such a methodology can be adapted to cavern design provided that the pressure, temperature, loading rate, etc. remain in the same ranges as those used for laboratory tests. As laboratory and *in situ* conditions may differ, there is already a problem, which can only grow more severe with the new issues associated with the energy transition.

Another issue with the classical design methodology comes from two different visions of rock salt, as a porous or a non-porous medium. Because of its very low hydraulic conductivity [34], studies often focus on the thermo-mechanical behavior, leaving out hydraulic phenomena, and consider salt as a non-porous medium, thus allowing the use of design criteria in terms of the total stress. A different approach [35] argues that the pressure in the cavern contributes to crack opening and propagation and thus considers the effective stress in the Terzaghi sense for the tensile criterion. This approach is much more conservative than the non-porous approach and is inconsistent with the fact that for dilatancy criteria, the distinction between total and effective stresses is never made, even in the presence of mean pressure.

Specifically concerning tensile criteria, an alternative to continuum mechanics is to use a continuum-discontinuum approach, via which crack creation and propagation can be considered. Unfortunately, this approach is unable to treat simultaneously and adequately a great number of cracks unless a time- and memory-consuming process is used, as shown in [36]. This approach, generally applied to brittle material, also cannot be used to simulate long-term cavern operation scenarios, in which the creep behavior is dominant. Furthermore, when large stresses are achieved in a relatively short time, a high density of evenly distributed cracks can be activated [36], which may justify a continuous approach addressing tensile zones rather than individual cracks.

Since the practical application of this work is salt cavern design, especially for storage purposes, we focus on early stages of damage development, in which the permeability remains extremely small and only microcracks are distributed through the rock mass. In this phase, there is no apparent macroscopic damage and no large-scale fractures develop. Therefore, a continuum medium approach is adopted, and hydraulic aspects are not considered in this study; rather only thermo-mechanical problems are discussed. The purpose of this work is to propose a unified approach to reconcile the creep laws and the design criteria. We present a new constitutive model consistent with a wide range of loadings, in terms of pressure, temperature, and loading rate, and able to address the new issues of the energy transition. The model focuses on three important phenomena: distortion creep, dilatancy, and tension. Viscoplastic strains associated with dilatancy and tension allow one to define design criteria, in terms of strains, and avoid any recourse to external criteria in post-processing and the incumbent inconsistencies. The evolution of damage zones around the cavern can therefore be better controlled, and considering a damaged volume instead of a damaged surface (the cavern wall) allows one to be less conservative and more accurate.

The paper is organized as follows. In Section 2, a constitutive model is developed, and the model is used in Section 3 to fit experimental data concerning distortion, dilatancy, and tension. In Section 4, a fully coupled thermo-mechanical code is used to simulate salt caverns and study the influence of cycling (amplitude, period, and mass flow). The study is conducted with two gases: the promising hydrogen is compared to the classical methane. In Section 5, the results are analyzed with the classical and new methodologies for comparison purposes, and the consequences of the addition of the dilatancy and tension phenomena on the cavern behavior are assessed.

2. Constitutive model

This section presents the development of a constitutive model, including design criteria, that is consistent with short- and long-term conditions. The model is based on the Lemaitre model [12] and enriched with the dilatancy and tension phenomena through a multi-mechanisms approach, thus allowing great flexibility in the depiction of phenomena. A first version of this model was presented in [37], considering only dilatancy, in a purely mechanical analysis. In this improved version, the tension phenomenon was added, in addition to thermo-mechanical coupling. Although micromechanical phenomena can provide valuable information on the true physical behavior of rock salt, this approach is purely phenomenological. This approach is based on laboratory testing at the macroscopic scale, with tested samples supposed to be the size of a representative elementary volume for the cavern.

2.1. Framework and definitions

The stress tensor, denoted by $\underline{\underline{\sigma}}$, can be decomposed into a deviatoric component and a spherical component[1]:

$$\underline{\underline{\sigma}} = \sqrt{2/3}\; q\; \underline{\underline{J}} - \sqrt{3}\; p\; \underline{\underline{I}} \tag{1}$$

where

$$\begin{aligned} p &= -\mathrm{tr}(\underline{\underline{\sigma}})/3, \qquad q = \sqrt{3/2}||\underline{\underline{\sigma}}'|| \\ \underline{\underline{J}} &= \underline{\underline{\sigma}}'/||\underline{\underline{\sigma}}'||, \qquad \underline{\underline{I}} = \underline{\underline{1}}/\sqrt{3} \end{aligned} \tag{2}$$

in which $\underline{\underline{\sigma}}'$ is the deviatoric stress tensor, p is the mean stress, and q is the von Mises equivalent stress. In the Haigh-Westergaard stress space, the position of the stress point in the deviatoric plane can be identified by the Lode angle $\theta \in [0, \pi/3]$, defined as

$$\theta = \tfrac{1}{3}\cos^{-1}(\sqrt{6}\;\mathrm{tr}\left(\underline{\underline{J}}^3\right)) \tag{3}$$

The triaxial extension state of stress corresponds to $\theta = 0$, and the triaxial compression state of stress corresponds to $\theta = \pi/3$.

Due to isotropy, the general form of any scalar isotropic function (plastic potential), which depends on the state of stress $\underline{\underline{\sigma}}$, can be expressed in terms of the three particular principal invariants (p, q, θ). Assuming that $f\left(\underline{\underline{\sigma}}\right) = P(p, q, \theta)$ is a smooth function, its gradient with respect to $\underline{\underline{\sigma}}$ can be obtained using the chain rule of differential calculus:

$$\partial_{\underline{\underline{\sigma}}} f = -\left(\sqrt{1/3}\;\partial_p P\right)\underline{\underline{I}} + \left(\sqrt{3/2}\;\partial_q P\right)\underline{\underline{J}} + \left(\sqrt{3/2}\;\partial_\theta P/q\right)\underline{\underline{K}} \tag{4}$$

where $\underline{\underline{K}}$ is given by

$$\underline{\underline{K}} = \left(\sqrt{2}\underline{\underline{I}} + \cos(3\theta)\underline{\underline{J}} - \sqrt{6}\underline{\underline{J}}^2\right)/\sqrt{1-\cos(3\theta)^2} \tag{5}$$

[1]For any tensor $\underline{\underline{a}}$, its deviatoric part is designated by a prime: $\underline{\underline{a}}' = \underline{\underline{a}} - \frac{1}{3}\mathrm{tr}(\underline{\underline{a}})\underline{\underline{1}}$, where $\underline{\underline{1}}$ is the identity tensor and tr(-) denotes the trace operator.

The three tensors $\underline{\underline{I}}$, $\underline{\underline{J}}$ and $\underline{\underline{K}}$ form an orthonormal basis for the subspace of the symmetric second-order tensors that are coaxial with $\underline{\underline{\sigma}}$ when $\underline{\underline{\sigma}}$ has three different eigenvalues. An alternative solution to using the three invariants (p, q, θ) of the stress tensor $\underline{\underline{\sigma}}$ is to use its principal values (σ_1, σ_2, σ_3) to express the function $f(\underline{\underline{\sigma}})$. In this case, the gradient of $f\left(\underline{\underline{\sigma}}\right) = G(\sigma_1, \sigma_2, \sigma_3)$ with respect to $\underline{\underline{\sigma}}$ can be expressed, in the basis ($\underline{\underline{I}}$, $\underline{\underline{J}}$, $\underline{\underline{K}}$), as

$$\partial_{\underline{\underline{\sigma}}} f = \left(\sqrt{1/3}\ X\right)\underline{\underline{I}} + \sqrt{3/2}(Y\cos\theta + Z\sin\theta)\underline{\underline{J}} + \sqrt{3/2}(Z\cos\theta - Y\sin\theta)\underline{\underline{K}} \tag{6}$$

with

$$X = G'_1 + G'_2 + G'_3, \qquad Y = (2G'_1 - G'_2 - G'_3)/3, \qquad Z = (G'_2 - G'_3)/\sqrt{3} \tag{7}$$

where $G'_i = \partial_{\sigma_i} G$. The basis ($\underline{\underline{I}}$, $\underline{\underline{J}}$, $\underline{\underline{K}}$) and the gradient calculations will be used to define the direction of the viscoplastic strain rate.

2.2. *Viscoplastic strain rate tensor*

We assume that the viscoplastic strain rate tensor, denoted $\dot{\underline{\underline{\varepsilon}}}_{vp}$, can be decomposed into compressive (c) and tensile (t) parts:

$$\dot{\underline{\underline{\varepsilon}}}_{vp} = \dot{\underline{\underline{\varepsilon}}}^c_{vp} + \dot{\underline{\underline{\varepsilon}}}^t_{vp} \tag{8}$$

The evolutions of both parts are to be treated separately. Regarding the compressive part, it can in turn be decomposed, following the classical decomposition between a deviatoric component, in the deviatoric plane, and a spherical component, in the hydrostatic direction:

$$\dot{\underline{\underline{\varepsilon}}}^c_{vp} = \sqrt{3/2}\ \dot{\gamma}^c_{vp}\underline{\underline{N}}^c - \sqrt{1/3}\ \dot{\zeta}^c_{vp}\underline{\underline{I}} \tag{9}$$

In this decomposition, the quantities $\dot{\gamma}^c_{vp}$ and $\dot{\zeta}^c_{vp}$ represent the viscoplastic distortion and volumetric strain, respectively, and are defined as follows:

$$\dot{\gamma}^c_{vp} = \sqrt{2/3}||\dot{\underline{\underline{\varepsilon}}}^{c\prime}_{vp}||, \qquad \dot{\zeta}^c_{vp} = -\mathrm{tr}(\dot{\underline{\underline{\varepsilon}}}^c_{vp}) \tag{10}$$

The unit tensor $\underline{\underline{N}}^c$ is used to define the deviatoric flow direction, which in this work is assumed to be defined in terms of the gradient of a potential function of the form $P(\underline{\underline{\sigma}}) = q/\varrho(\theta)$. Using Equation 4, the tensor $\underline{\underline{N}}^c$ can then be written as

$$\underline{\underline{N}}^c = \partial_{\underline{\underline{\sigma}}}P/||\partial_{\underline{\underline{\sigma}}}P|| = \left(\underline{\underline{J}} - (\varrho'/\varrho)\underline{\underline{K}}\right)/\sqrt{1 + (\varrho'/\varrho)^2} \tag{11}$$

where $\varrho'(\theta) = \mathrm{d}\varrho/\mathrm{d}\theta$. The function $\varrho(\theta)$ allows accounting for differences in the material behavior between triaxial extension and triaxial compression by defining the size and shape of the deviatoric section of the potential $P(\underline{\underline{\sigma}})$. The following expression proposed in [38] is used:

$$\varrho(\theta) = \frac{\cos\left(\frac{1}{3}\arccos(\text{-}\chi)\right)}{\cos\left(\frac{1}{3}\arccos(\chi\cos 3\theta)\right)} \tag{12}$$

where $\chi \in [0, 1[$ is a constant parameter. The function $\varrho(\theta)$ is defined for $\theta \in [0, \pi/3]$ and extended by symmetry to $[0, 2\pi]$. Examples of deviatoric sections are shown in Figure 1a.

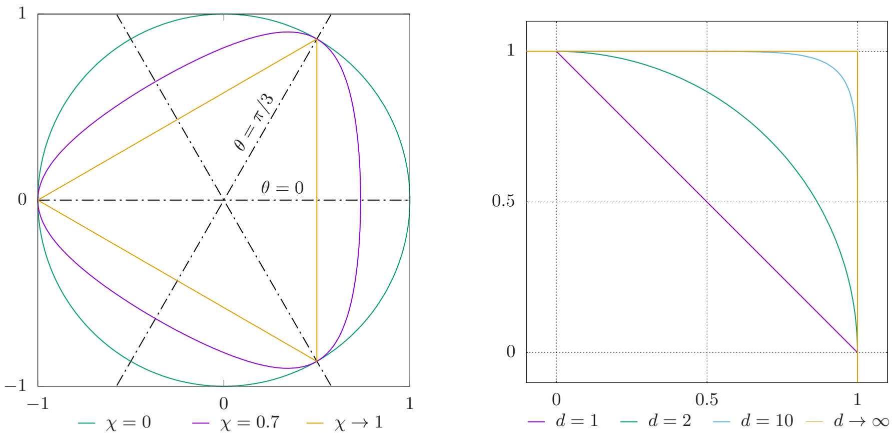

(a)

(b)

Figure 1: Cross-section of the potential $P(\underline{\underline{\sigma}})$ with the deviatoric plane for three values of χ (a) and cross-section of the potential $G(\underline{\underline{\sigma}})$ with the plane $\sigma_3 = 0$ for four values of d (b).

Regarding the tensile part, we consider a Rankine-type mechanism:

$$\underline{\underline{\dot{\varepsilon}}}^t_{vp} = \dot{\lambda}\partial_{\underline{\underline{\sigma}}} G \tag{13}$$

with

$$G(\underline{\underline{\sigma}}) = \left(\langle\sigma_1\rangle^d + \langle\sigma_2\rangle^d + \langle\sigma_3\rangle^d\right)^{1/d} = \sigma_+ \tag{14}$$

where $\langle\cdot\rangle$ are the Macaulay brackets, *i.e.*, $\langle x\rangle = (x + |x|)/2$. The constant parameter $d \geq 1$ controls the shape of the potential surface [39, 40], as can be observed from Figure 1b. For $d = 2$, the surface is a spherical sector, and when d tends to infinity, it tends to a Rankine-type model. Although the expression of $G(\underline{\underline{\sigma}})$ encourages working with the basis associated with the principal values (σ_1, σ_2, σ_3), the tensile viscoplastic strain rate $\dot{\underline{\underline{\varepsilon}}}^t_{vp}$ is written in the basis ($\underline{\underline{I}}$, $\underline{\underline{J}}$, $\underline{\underline{K}}$) for consistency with the compressive component. In this basis, we can isolate the deviatoric and the spherical components:

$$\dot{\underline{\underline{\varepsilon}}}^t_{vp} = \sqrt{3/2}\ \dot{\gamma}^t_{vp}\underline{\underline{N}}^t - \sqrt{1/3}\ \dot{\zeta}^t_{vp}\underline{\underline{I}} \tag{15}$$

The quantities $\dot{\gamma}^t_{vp}$ and $\dot{\zeta}^t_{vp}$ are defined as follows, using Equation 7:

$$\dot{\gamma}^t_{vp} = \dot{\lambda}\sqrt{Y^2 + Z^2}, \qquad \dot{\zeta}^t_{vp} = -\dot{\lambda}X \tag{16}$$

where in this case, the principal values G'_i of $\partial_{\underline{\underline{\sigma}}} G$ are

$$G'_i = \langle \sigma_i/\sigma_+ \rangle^{d-1} \tag{17}$$

Using Equation 6, the direction $\underline{\underline{N}}^t$ is

$$\underline{\underline{N}}^t = \Big((Y\cos\theta + Z\sin\theta)\underline{\underline{J}} + (Z\cos\theta - Y\sin\theta)\underline{\underline{K}} \Big) / \sqrt{Y^2 + Z^2} \tag{18}$$

Finally, by adding the compressive and tensile components from Equations 9 and 15, we obtain an expression for the viscoplastic strain rate tensor:

$$\dot{\underline{\underline{\varepsilon}}}_{vp} = \sqrt{3/2}\ (\dot{\gamma}^c_{vp}\underline{\underline{N}}^c + \dot{\gamma}^t_{vp}\underline{\underline{N}}^t) - \sqrt{1/3}\ (\dot{\zeta}^c_{vp} + \dot{\zeta}^t_{vp})\underline{\underline{I}} \tag{19}$$

In the following, the different components of the viscoplastic strain rate tensor, $\dot{\gamma}^c_{vp}$, $\dot{\gamma}^t_{vp}$, $\dot{\zeta}^c_{vp}$, and $\dot{\zeta}^t_{vp}$, will be referred to as the compressive distortion, tensile distortion, compressive volumetric, and tensile volumetric strain rates, respectively. To fully define the evolution of the viscoplastic strain rate, the variables $\dot{\gamma}^c_{vp}$, $\dot{\zeta}^c_{vp}$, and $\dot{\lambda}$ still need to be defined, which will be done in the following section.

2.3. Internal variables

We assume that the material past history is represented by the viscoplastic distortion γ^c_{vp} and the viscoplastic tensile strain λ. The local thermodynamic state can thus be defined by ($\underline{\underline{\sigma}}, T, \gamma^c_{vp}, \lambda$). We also assume that the ratio $\mathrm{d}\zeta^c_{vp}/\mathrm{d}\gamma^c_{vp}$ depends only on this thermodynamic state. These hypotheses allow us to write $\dot{\gamma}^c_{vp}$, $\dot{\zeta}^c_{vp}$ and $\dot{\lambda}$ as:

$$\dot{\gamma}^c_{vp} = \dot{\gamma}^c_{vp}(\underline{\underline{\sigma}}, T, \gamma^c_{vp}, \lambda), \qquad \dot{\zeta}^c_{vp} = \varphi(\underline{\underline{\sigma}}, T, \gamma^c_{vp}, \lambda)\dot{\gamma}^c_{vp}, \qquad \dot{\lambda} = \dot{\lambda}(\underline{\underline{\sigma}}, T, \gamma^c_{vp}, \lambda) \tag{20}$$

with $\varphi(\underline{\underline{\sigma}}, T, \gamma_{vp}^c, \lambda)$ a function to be defined. Note that this definition of $\dot{\zeta}_{vp}^c$ implies that the viscoplastic volumetric strain only varies if there is an evolution in the distortion.

The evolution of γ_{vp}^c is a generalization of Lemaitre model, supplemented by the effect of the mean pressure p and the Lode angle θ:

$$\frac{\mathrm{d}(\gamma_{vp}^c)^{1/a}}{\mathrm{d}t} = \left\langle \frac{q/\varrho(\theta) - (\gamma_{vp}^c)^b Bp - C}{K} \right\rangle^{k/a} \tag{21}$$

where the mean pressure is taken into account through the term $(\gamma_{vp}^c)^b Bp$: no evolution of γ_{vp}^c can occur as long as $q/\varrho(\theta) - (\gamma_{vp}^c)^b Bp \leq C$. The influence of θ is taken into account by the function ϱ (defined in Equation 12), which adds asymmetry in the hardening: all else being equal, the viscoplastic strain is greater in extension than in compression. Equation 21 can be reduced to Lemaitre evolution law by setting $\chi = 0$ and $B = 0$.

The evolution of ζ_{vp}^c is defined through the function φ:

$$\varphi(\underline{\underline{\sigma}}, T, \gamma_{vp}^c, \lambda) = \min\left(v \frac{\Big(\langle p \rangle / N\Big)^n - \gamma_{vp}^c}{\Big(\langle p \rangle / M\Big)^m + \gamma_{vp}^c}, V \right) \tag{22}$$

where the sign of $\Big(\langle p \rangle / N\Big)^n - \gamma_{vp}^c$ determines whether the behavior is contracting or dilating. The parameter V is a threshold to prevent excessive volumetric strains under low mean stresses.

The evolution of λ is defined as follows:

$$\dot{\lambda} = \Lambda \left\langle \frac{\sigma_+ - R}{S e^{-\omega \lambda}} \right\rangle^s \tag{23}$$

where the modulus R is an equivalent tensile strength, such that no tensile strains occur as long as σ_+ remains below this threshold. Attention is drawn to the particular case $R = 0$, in which there is no threshold for tensile strains, by similarity to compression, for which it is commonly admitted that there is no creep threshold ($C = 0$).

In Equations 21 through 23, the constants a, k, b, B, C, n, N, m, M, v, V, Λ, R, s, S, and ω are material parameters. The moduli K, M, N, and S may depend on the temperature. Here, we make the assumption that it is only the case for K and consider that it follows Arrhenius law:

$$K(T) = K_r e^{A(\frac{1}{T} - \frac{1}{T_r})} \tag{24}$$

where K_r and A are material constants and T_r a reference temperature.

3. Calibration of the rheological parameters

A few examples of fittings of laboratory tests performed in our facilities are presented: three short-term triaxial tests, with constant confining pressures of 5, 10 and 15 MPa and an axial strain rate of 5×10^{-6} s^{-1}; one multi-stage creep test with a constant confining pressure of 5 MPa and deviatoric stresses of 5, 10 and 15 MPa; and one Brazilian test performed with a loading rate of 8×10^{-7} s^{-1}.

Samples were retrieved from a salt dome in the Landes (South West of France) at a depth of 1350 m. The samples were cut into cylindrical specimens with a diameter of 65 mm and a height-to-diameter ratio of 2 for all triaxial tests (short-term and creep) and 1/2 for the Brazilian tests. Before all triaxial tests, the specimens were subjected to isotropic loading corresponding to the intended confining pressure for a duration of a day. The specimen used for the Brazilian test was not subjected to any preconditioning. During all triaxial tests, the axial strain is deduced from an LVDT measurement of the relative displacement of the specimen ends. During the short-term triaxial tests, the volumetric strain is deduced from the measurement of the volume change of the confining oil. During the Brazilian test, the vertical and horizontal diametrical displacements were measured by means of two LVDT sensors. All tests were performed at room temperature.

For all triaxial tests, all end effects and potential sample heterogeneity are neglected, and the samples are considered to remain perfect cylinders at all times. Consequently, no tensile stresses are to develop in the sample and all components of the rheological model related to tension are zero. This assumption allows us to consider that the total volumetric strain $\zeta = -\mathrm{tr}(\underline{\underline{\varepsilon}})$, with $\underline{\underline{\varepsilon}}$ the total strain tensor, can be deduced from the change in the volume of the confining oil. Regarding the distortion component of the strain tensor $\gamma = \sqrt{2/3}||\underline{\underline{\varepsilon}}'||$, it can be computed as $\gamma = -\varepsilon_z - \zeta/3$, with ε_z the axial strain. We can then proceed with a direct fitting procedure for all parameters related to elasticity, distortion and dilatancy. The elastic parameters are first fitted using the unloading/loading cycles of the three short-term triaxial tests. The elastic distortion and volumetric strains can then be computed and subtracted from the measured total distortion and volumetric strains to obtain the compressive viscoplastic distortion and volumetric strains $\gamma_{vp}^c = \gamma - \gamma_e$ and $\zeta_{vp}^c = \zeta - \zeta_e$. The parameters related to the compressive mechanisms are then fitted using both the short-term triaxial tests and the long-term creep test. The parameters are fitted in two independent steps: the parameters related to the Lemaitre-type hardening mechanism with γ_{vp}^c, and the parameters related to dilatancy with ζ_{vp}^c. Although the expression of ζ_{vp}^c includes γ_{vp}^c, experimental values of γ_{vp}^c are used in the fitting of ζ_{vp}^c, thus ensuring the independence of the two fits. Since all tests were performed in a compression state of stress, the parameter χ, related to the differences in the behavior of rock salt in compression and extension states of stress, could not be fitted. Likewise, all tests were performed at the same constant temperature, preventing fitting parameters A and T_r. They are set to values from the MINES ParisTech laboratory database.

The parameters related to tension are fitted based on the Brazilian test results. Naturally, the assumption of uniformly strained samples cannot be made in this case. The Brazilian test is simulated numerically with a FEM code, and the parameters related to tension are fitted by trial and error, by comparing the numerical simulation results with the vertical and horizontal diametrical displacements measured by the LVDT sensors. The parameter R is set to zero for consistency with compression without any cohesion ($C = 0$). All other parameters are set to the previously adjusted values on triaxial tests.

All the fits can be oberved in Figure 2, and the fitted parameters are reported in Table 1. The quality of the fits is very encouraging. Naturally, they could be improved to nearly perfect fits if the tests were fit independently. Here, the fitting procedure is global, and all tests are fit with a single parameter set.

Following the classical methodology to design a salt cavern, dilatancy and tensile criteria can be fitted based on the triaxial tests and the Brazilian test, respectively. A dilatancy criterion is fitted on the onset of dilatancy for the short-term triaxial tests, *i.e.*, the moment

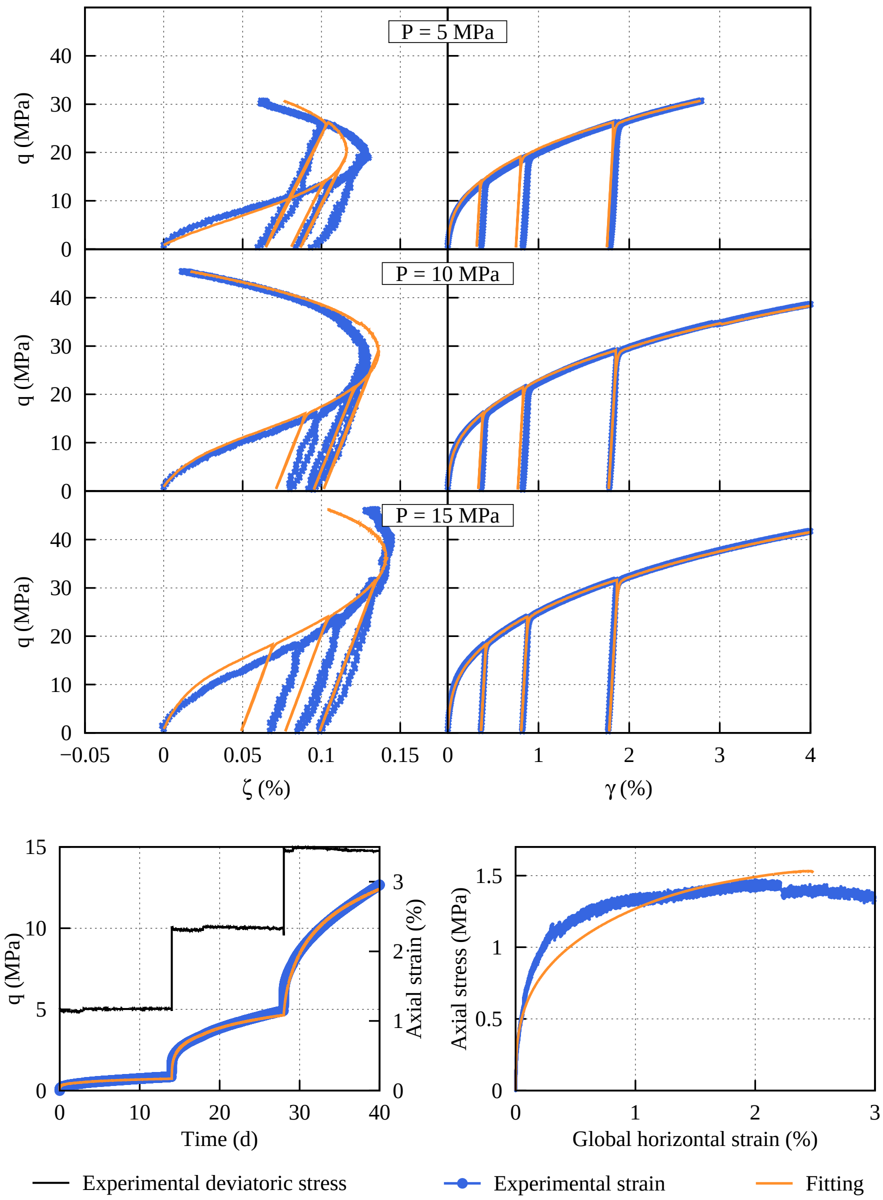

Figure 2: Fitting of the rheological parameters based on three triaxial tests, one multistage creep test, and one Brazilian test (the global horizontal strain is computed by dividing the horizontal diametrical displacement by the initial sample diameter).

when the viscoplastic volumetric strain rate changes sign. The data from the three short-term triaxial tests from Figure 2 are used, in addition to nine other similar tests from

Elasticity		**Distortion**						
E	ν	a	k	K_r	b	B	C	χ
28800	0.32	0.29	2.2	0.13	0.24	0.044	0	0.7
Temperature		**Dilatancy**						
A	T_r	v	n	N	m	M	V	
909	300	0.080	1.3	0.012	3.3	1.37	1	
Tension								
Λ	R	S	ω	d	s			
5×10^4	0	1	1×10^{-8}	10	1			

Table 1: Parameters used to fit both short-term and creep tests on Landes salt (units in μm/m, MPa, K and d).

the same experimental campaign. Figure 3 shows the experimental points corresponding to the onset of dilatancy plotted in the stress space and a linear fitted dilatancy criterion ($q = 1.3p + 2.5$) that correctly reproduces the data. A tensile criterion is fitted based on the Brazilian test: the maximum axial stress provides the tensile strength ($\sigma_1 = R_T = 1.4$ MPa).

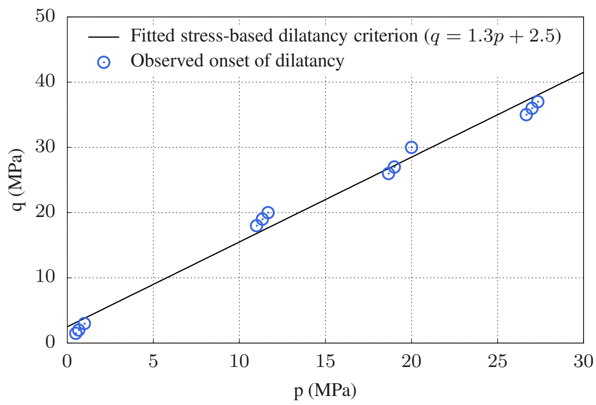

Figure 3: Fitting of a dilatancy criterion on the onset of dilatancy of 12 short-term triaxial tests.

4. Method

We consider a salt cavern under cyclic loading conditions, in a fully integrated approach. Instead of arbitrarily imposing a cavern temperature and a pressure as boundary conditions for the thermo-mechanical problem in rock salt, the cavern thermodynamics is taken into account, and both problems are fully coupled. This approach allows rigorously simulating the storage of different gases in the cavern, with different thermodynamic behaviors.

4.1. Fully coupled problem

The system is divided into two subsystems: the cavern, and the surrounding formations. The cavern is spherical, the surrounding formation is homogeneous and infinite, and only one fluid is present in the cavern, with no brine or insoluble materials. The initial temperature and pressure are homogeneous in the cavern and in the surrounding formation. The governing equations for both subsystems, in addition to constitutive equations for the surrounding formation, allow computing the cavern thermodynamics and the rock salt thermomechanical behavior with a fully coupled approach.

First, the cavern governing equations express the variations in the pressure P and temperature T, which are supposed to be homogeneous in the cavern, based on the mass of fluid in the cavern $\mathcal{M}$, the volume of the cavern $\mathcal{V}$, and heat transfers from the injection/withdrawal well and the surrounding rock salt. The cavern governing equations can be written as

$$\begin{pmatrix} \alpha & -\beta \\ \mathcal{M}C_p & -\mathcal{V}\alpha T \end{pmatrix} \begin{pmatrix} \dot{T} \\ \dot{P} \end{pmatrix} = \begin{pmatrix} \dot{\mathcal{V}}/\mathcal{V} - \dot{\mathcal{M}}/\mathcal{M} \\ \Psi_R + \Psi_I \end{pmatrix} \tag{25}$$

where $\alpha(P,T)$, $\beta(P,T)$, and $C_P(P,T)$ are the isobaric thermal expansion coefficient, the isothermal compressibility factor, and the specific heat capacity at constant pressure, respectively. Concerning the heat transfers, Ψ_R is the heat exchanged between the cavern and the surrounding rock salt, and $\Psi_I = Q_I(H_I - h)$ is the heat resulting from the in-going matter, with Q_I the inflow rate and $H_I(P,T)$ and $h(P,T)$ the specific enthalpy of the in-going matter and the matter in the cavern, respectively [41].

The thermodynamic problem in the cavern in terms of pressure and temperature is used as boundary conditions in the surrounding rock salt problem in the rock salt, expressed by the following thermo-mechanical governing equations:

$$\begin{aligned} \partial_r \sigma_r + \frac{2}{r}(\sigma_r - \sigma_\theta) &= 0 \\ \partial_r^2 T + \frac{2}{r}\partial_r T &= \frac{\rho C_\sigma}{\kappa}\dot{T} \end{aligned} \tag{26}$$

where $r = r(r_0, t)$ is the current position of the material point initially at radius r_0, σ_r and σ_θ refer to the radial and tangential components of the stress tensor $\underline{\underline{\sigma}}$, respectively, ρC_σ is the volumetric heat capacity, and κ is the isotropic thermal conductivity.

Equation 26 must be supplemented by a constitutive law describing the rock salt behavior. The spherical symmetry allows limiting the equations to the logarithmic strains in the radial and tangential directions defined by $H_r = \ln(\partial_{r_0} r)$ and $H_\theta = \ln(r/r_0)$, respectively:

$$\begin{aligned} \dot{H}_r &= \frac{1+\nu}{E}\dot{\sigma}_r - \frac{\nu}{E}\mathrm{tr}(\dot{\underline{\underline{\sigma}}}) + \alpha_\ell \dot{T} + \left(\dot{\underline{\underline{\varepsilon}}}_{vp}\right)_r \\ \dot{H}_\theta &= \frac{1+\nu}{E}\dot{\sigma}_\theta - \frac{\nu}{E}\mathrm{tr}(\dot{\underline{\underline{\sigma}}}) + \alpha_\ell \dot{T} + \left(\dot{\underline{\underline{\varepsilon}}}_{vp}\right)_\theta \end{aligned} \tag{27}$$

where the subscripts r and θ refer to the radial and tangential components, respectively, E is Young's modulus, ν is Poisson's ratio, and α_ℓ is the coefficient of linear thermal expansion. In each direction, the first terms correspond to the elastic and thermal strains; in the last term, $\dot{\underline{\underline{\varepsilon}}}_{vp}$ is the viscoplastic strain rate defined in Section 2.

4.2. Numerical simulations

All numerical simulations were performed with the code DEMETHER (MINES ParisTech, Paris, France), developed in a thermodynamically consistent framework for underground salt cavern storage [41]. More specifically, Equations 25 through 27 are sequentially solved at each time step using an Euler implicit scheme in time and classical 1D finite elements in space. A total of 1000 second-order elements were used, their size increasing in a geometrical ratio from the cavern wall. No localization problem was encountered. The sensitivity to the mesh size was studied and no effect was noted, which can be explained by the one-dimensional problem, ensuring the absence of bifurcation issues, and the time-dependent behavior, allowing regularizing the solution.

A spherical cavern filled with gas and the surrounding rock salt are simulated. The initial radius of the cavern is 40 m, which amounts to a volume of approximately 270,000 m^3. The cavern is initially in equilibrium with the surrounding rock salt. The initial pressure and temperature in the whole system are $P = 22$ MPa and $T = 40$ °C, respectively, which can correspond to conditions near a depth of 1000 m. The mass flow in and out of the cavern is imposed; the pressure and temperature vary as a result of gas injection or withdrawal. Several simulations are performed, differing in terms of the nature of the gas in the cavern and the history of gas injection and withdrawal.

Concerning the nature of the gas in the cavern, two pure gases are considered: methane (CH_4) and hydrogen (H_2). Methane is the main component of natural gas, which has been stored for decades in salt caverns. In the energy transition context, hydrogen is one of the most promising gases for the storage of new forms of energy. Its storage in salt caverns is the subject of extensive research and development today regarding its technical [42] and economic [43, 44] feasibility. Yet, methane and hydrogen exhibit contrasting thermodynamic behaviors [45]. Using special high-accuracy equations of state for each gas (Setzmann and Wagner [46] for methane, and Kunz and Wagner [47] for hydrogen), we compare both gases. In terms of the Joule-Thomson coefficient $\partial_P T(h, P)$, both gases are radically different: for methane, $\partial_P T(h, P) > 0$ and for hydrogen, $\partial_P T(h, P) < 0$, as illustrated in Figure 4a, which shows that during an isenthalpic expansion, methane cools down whereas hydrogen heats up. Methane and hydrogen also differ regarding their compressibility behavior, as illustrated by Figure 4b, showing the mass of fluid that can be stored in a given volume as a function of the storage depth, when assuming a linear dependence between the initial state and the depth z in the form $P(z) = 0.022z$ (MPa) and $T(z) = 10 + 0.03z$ (°C). This mass is normalized with respect to methane at a depth of 1000 m ($P_0 = 22$ MPa, $T_0 = 40$ °C), according to the simple formula $\mathcal{M}/\mathcal{M}_0 = \rho(P(z), T(z))/\rho_{CH_4}(P_0, T_0)$. In a given volume, up to 10 times more methane than hydrogen (in terms of mass) can be stored.

Concerning the viscoplastic parameters, we use the ones fitted in Section 3 (Table 1). For each scenario and each gas, two types of simulations are performed: ($v = 0$, $\Lambda = 0$), and ($v \neq 0$, $\Lambda \neq 0$). Setting v and Λ to zero cancels out the compressive volumetric

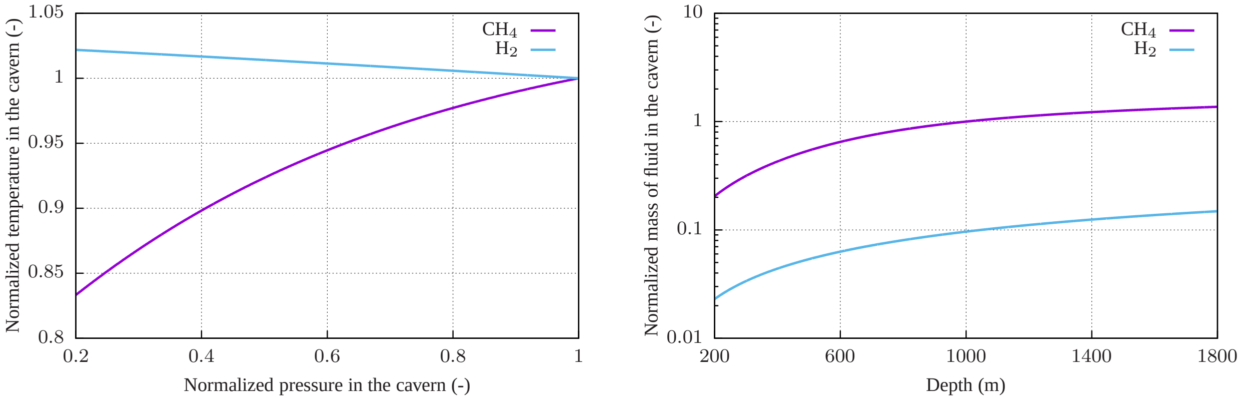

(a) Evolution of the temperature as a function of the pressure normalized with respect to T_0 and P_0, respectively, during an isenthalpic expansion from $P_0 = 22$ MPa, $T_0 = 40$ °C to $P = 0.2P_0$.

(b) Mass of fluid held in the same volume, as a function of the depth, normalized with respect to methane at a depth of 1000 m ($P_0 = 22$ MPa, $T_0 = 40$ °C).

Figure 4: Difference in the thermodynamic behaviors of methane and hydrogen.

strains and tensile strains, respectively. The influence of both components will be studied in Section 5.3. The thermal parameters are $\alpha_\ell = 4 \times 10^{-5}$ K^{-1}, $\kappa = 6$ W m^{-1} K^{-1}, and $\rho C_\sigma = 2 \times 10^6$ J m^{-3} K^{-1}.

Concerning the history of gas injection and withdrawal, it is imposed in terms of mass flow as a percentage of the initial mass of gas in the cavern. Although the initial mass is different for the methane and hydrogen, this approach allows defining the same history for both gases. All studied scenarios start with the withdrawal of 50% of the initial gas mass over a period of 60 days. Then, cycles are simulated, consisting of a phase of gas withdrawal, a phase of injection, and rest at 50% of the initial mass. Seven scenarios are studied. In the base-case scenario, the cycles range between 20 % and 80 % of the initial mass, and they last 180 days. The history of the mass of gas in the cavern can be observed in Figure 5. Two scenarios keep the cycling amplitude unchanged and reduce the cycle duration to 90 and 60 days by increasing the mass flow (see Figure 5a). These constant-amplitude scenarios are in line with the trend of the energy transition to accelerate the storage cycles and allow studying the effect of the cycling rate. Two scenarios keep the cycling rate unchanged and reduce the amplitude to 35-65 % and 40-60 % of the initial mass (see Figure 5b). These scenarios allow studying the effect of the cycling amplitude, all else being equal. The last two scenarios keep the mass flow unchanged, reduce the cycle duration to 90 and 60 days, and reduce the amplitude to 35-65 % and 40-60 % (see Figure 5c). These constant-mass-flow scenarios allow studying the differences between performing one large cycle or several small ones, while keeping the same amount of gas withdrawn from the cavern over each 180 day period. The cycles are repeated for a total duration of 20 years.

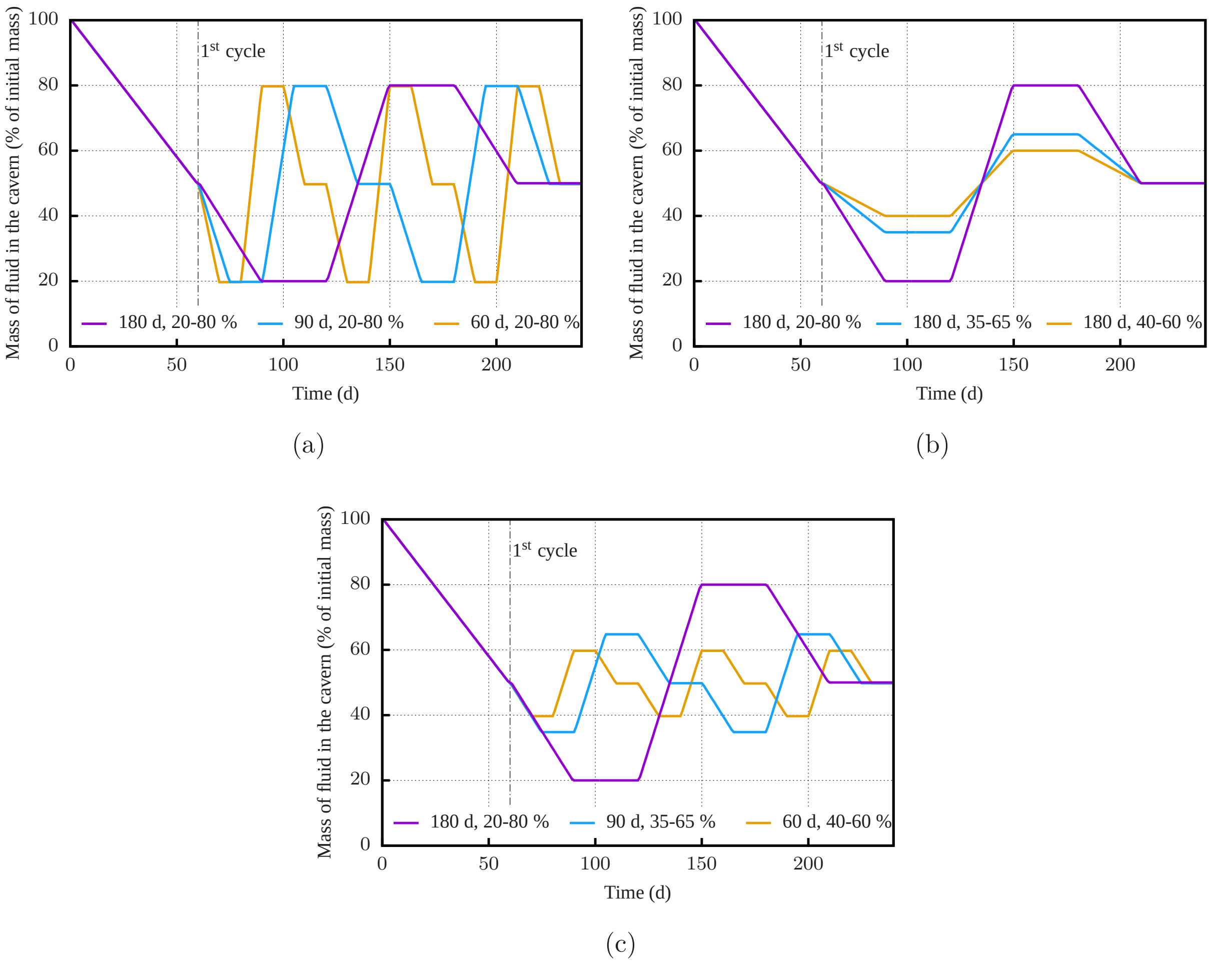

Figure 5: History of the mass of fluid in the cavern (first 240 days) for the constant-amplitude scenarios (a), the constant-cycling rate scenarios (b), and the constant-mass flow scenarios (c).

4.3. Dilatancy and tensile criteria

The results are to be analyzed in terms of the dilatancy and tension, using both a classical and a new approach. The classical approach uses the stress-based criteria defined in Section 3 in terms of dilatancy ($q = 1.3p + 2.5$) and tension ($\sigma_1 = R_T = 1.4$ MPa). As stated in the introduction, such criteria purely based on stress are widely used in salt cavern design. The criteria are used in post-processing, to assess the feasibility of a cavern simulated with any independent rheological model. The mere juxtaposition of such criteria, derived from short-term tests, and rheological laws, based on long-term creep tests, causes potential inconsistencies in the methodology.

The new approach is also based on the dilatancy and tension phenomena; however, instead of using stress-based criteria, it uses the internal variables introduced in the new rheological model to define strain-based criteria consistent with short- and long-term conditions. The first criterion, corresponding to the dilatancy onset, is $\dot{\zeta}^c_{vp} = 0$, where ζ^c_{vp} is the internal variable describing the evolution of the compressive part of the viscoplastic volumetric strain (see Equation 22). The second criterion, corresponding to the onset of the tensile mechanism, is $\lambda = 0$, where λ is the internal variable accounting for tensile strains (see Equation 23). As opposed to the classical stand-alone rate-intependent criteria, these new criteria are fully integrated into the rheological model and depend on the loading history, therefore allowing to follow dilatancy and tension at any point in time and space by studying the evolution of the internal variables.

5. Results and discussion

5.1. Cavern pressure and temperature

As a result of the imposed mass flow variations, as described in the scenario in Section 4.2, the pressure and temperature in the cavern exhibit cyclic variations. It is first worth mentioning that the results are the same whether v and/or Λ are zero, meaning that the cavern pressure and temperature are not affected by dilatancy or tension.

Figure 6 shows the evolution of the pressure and the temperature in the cavern for methane and hydrogen, for all scenarios, over the last 180 days. In the base-case scenario, the cavern pressure varies between 5 and 20 MPa, that is, between 22 and 90% of the geostatic pressure. All else being equal, the pressure amplitude is smaller when the cycle amplitude is smaller and slightly larger when the cycle duration is shorter. The results in terms of pressure are very similar for both gases because the mass flow variation is the same; this is not the case for temperature.

The temperature varies between 10 and 55 °C for methane in the base-case scenario. The temperature amplitude is larger when the cycle amplitude is smaller and significantly larger when the cycle duration is shorter. For hydrogen, the same trends can be observed, but the temperature range for every scenario is smaller (30 to 65 °C in the base-case scenario) and shifted up by 5 to 20 °C.

These results show that when considering only the global cavern performances in terms of pressure and temperature, all the imposed loading conditions seem acceptable, since they do not generate excessive variations. However, the mechanical stability of the cavern should be discussed as well, which will be done in the next section.

5.2. Dilatancy and tensile criteria

Design criteria are used to determine under what conditions the simulated caverns could be operated. This issue will be studied with both the classical and the new methodologies.

5.2.1. Classical methodology

Since the classical methodology deals addresses stress-based criteria, numerical simulations are performed with ($\upsilon = 0$, $\Lambda = 0$). When $\upsilon \neq 0$ or $\Lambda \neq 0$, the stress state at the cavern wall is modified by the developing viscoplastic strains. In particular, when $\Lambda \neq 0$, viscoplastic tensile strains develop, and σ_1 never becomes positive.

For the dilatancy criterion ($q = 1.3p + 2.5$), Figures 7a, 7c and 7e show the maximum value of $q - 1.3p$ per cycle at the cavern wall as a function of time, in addition to the constant $c = 2.5$ MPa. The dilatancy criterion is often exceeded ($q - 1.3p > c$) after a small number of cycles, except for the most conservative scenarios. For methane, in the constant-amplitude scenarios, the criterion is always exceeded after the first cycle (Figure 7a). For long cycles and small cycling amplitudes, the criterion is exceeded after fifteen years or even never (7c).

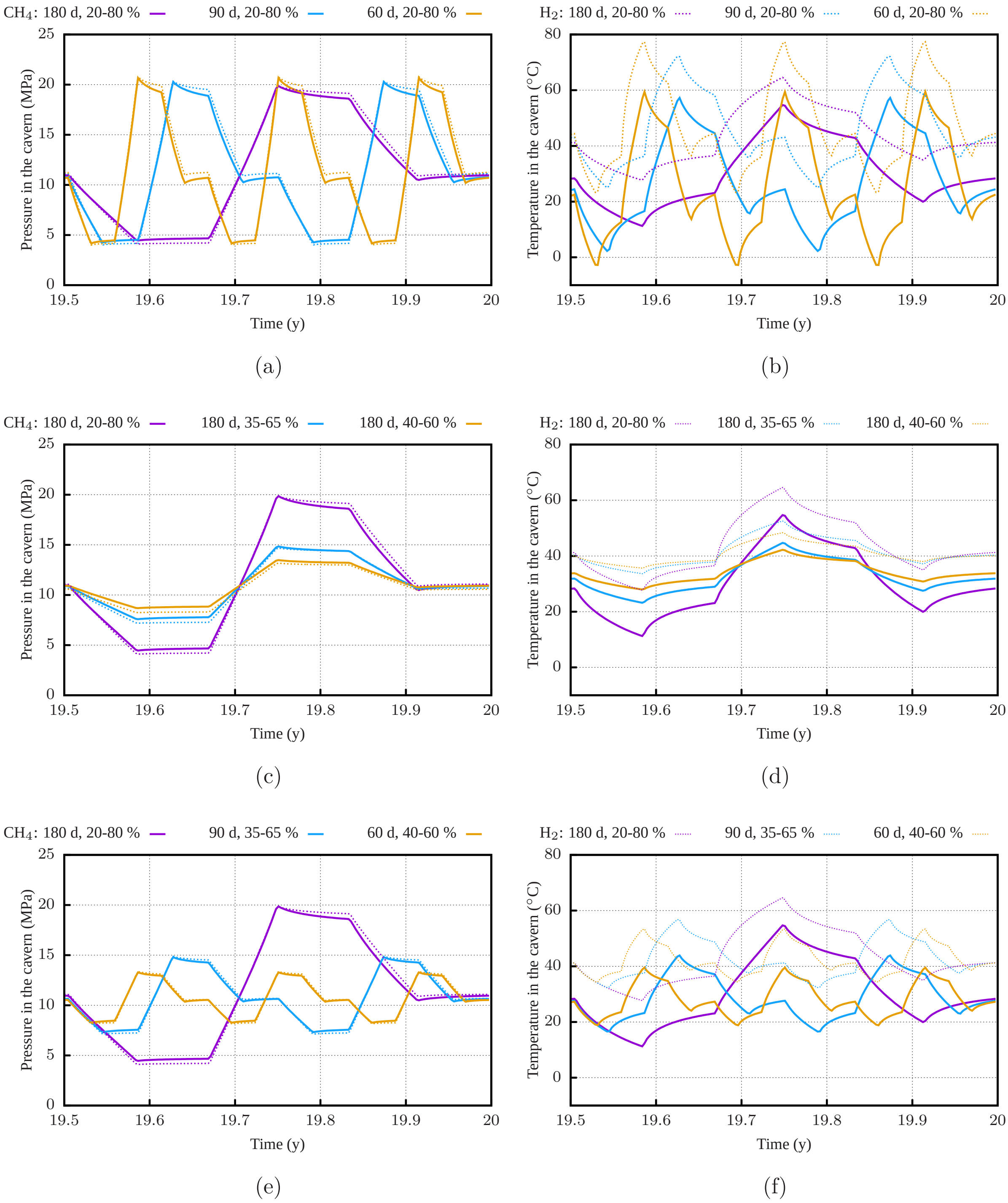

Figure 6: Evolution of the pressure (left) and temperature (right) in the cavern for methane and hydrogen for all scenarios (last 180 days).

However, even for small cycling amplitudes, short cycles lead to exceeding the criterion (Figure 7e). For hydrogen, it is always reached later than for methane, although the same trends can be observed for both gases.

For the tensile criterion ($\sigma_1 = R_T = 1.4$ MPa), Figures 7b, 7d and 7f show the maximum value of σ_1 per cycle at the cavern wall as a function of time, in addition to the constant $R_T = 1.4$ MPa. The tensile criterion is always exceeded ($\sigma_1 > R_T$) later than the dilatancy criterion. For methane, in the base-case scenario, the tensile criterion is exceeded after approximately seven years and as soon as the second cycle for shorter cycles (Figure 7b). For long cycles and small cycling amplitudes, it is never exceeded (Figure 7d). In turn, even for small cycling amplitudes, short cycles lead to exceeding the criterion or moving towards it (Figure 7f). Similarly to the dilatancy criterion, the tensile criterion is always reached sooner for methane than for hydrogen, but both gases exhibit similar behaviors.

These classical dilatancy and tensile criterion are very conservative. Except for the scenarios with the smallest amplitudes, the criteria are always easily exceeded, often during the very first cycles of the cavern operation. With this methodology, as soon as the cavern wall reaches the criterion, the cavern operation is discouraged, which is very restrictive. Moreover, since the creep law is determined independently from these criteria, it is not very sensible to study the stress state at the cavern wall when the criteria are significantly exceeded. It is reasonable to assume that the stress state is altered in the dilatancy or tension zones. Under these conditions, whether a cavern should be operated is not straightforward, which raises questions about the classical methodology and the determination of the criteria. Whereas creep laws are strongly time-dependent, design criteria are only fitted based on short-term tests and supposed to be time-independent. Why should these boundaries be intrinsic, and could they not depend on the loading rate? The new methodology is proposed to overcome these limitations.

5.2.2. New methodology

When using the new rheological model with ($v \neq 0$, $\Lambda \neq 0$), dilatancy and tensile phenomena can be analyzed by considering the internal variables ζ^c and λ. In the present

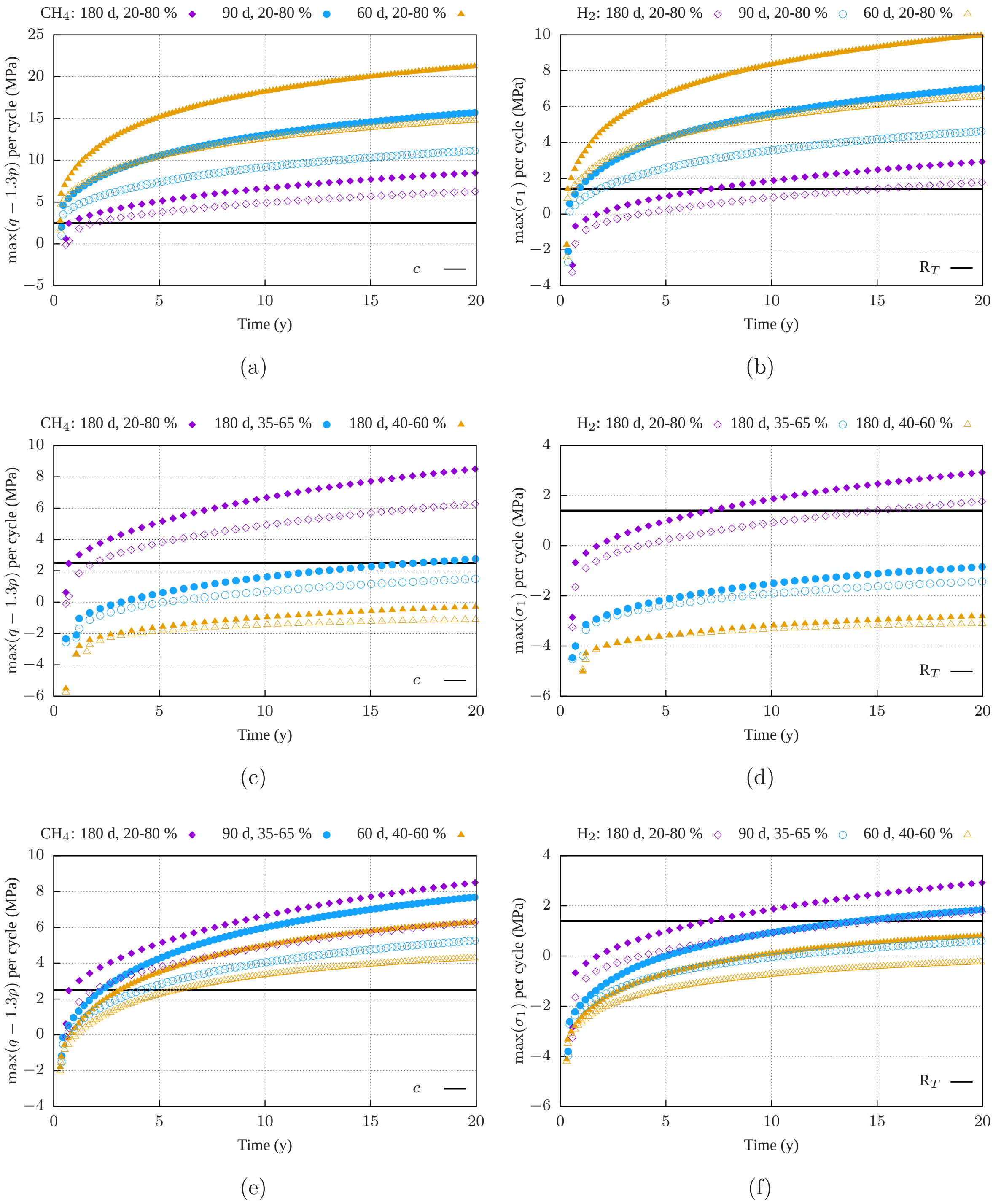

Figure 7: At the cavern wall and for each cycle, maximum value of $q - 1.3p$ compared with $c = 2.5$ MPa (left) and maximum value of σ_1 compared with $R_T = 1.4$ MPa (right), for methane and hydrogen in all scenarios.

study, we choose the dilatancy criterion $\dot{\zeta}^c_{vp} = 0$ and the tensile criterion $\lambda = 0$, as described in Section 4.3. Dilatancy and tension are analyzed in terms of both extent and magnitude. For the extent, we study the dilatancy and tensile zones, defined as all points at which the corresponding criterion is exceeded. Their width is expressed as a percentage of the cavern radius: $(r_{max}/r_{cav} - 1) \times 100$, where r_{max} is the largest radius for which the criterion is exceeded and r_{cav} is the cavern radius. For the magnitude, we consider the values of viscoplastic volumetric strains associated with each phenomenon at the cavern wall: ζ^c_{vp} for dilatancy and ζ^t_{vp} for tension.

As opposed to the classical dilatancy criteria, the criterion $\dot{\zeta}^c = 0$ is not fixed on the stress space but rather depends on the loading history. Figure 8 shows for both gases and all scenarios the evolution of the width of the dilatancy zone and the history of ζ^c_{vp} at the cavern wall. For all simulations, dilatancy appears after a small number of cycles, as was observed with the classical methodology. Simulations with methane always predict smaller dilatancy zones than ones with hydrogen. These results are different from those obtained with the classical methodology, which can be explained by the fact that the criteria are based on very different hypotheses.

Figures 8a, 8c and 8e show that the size of the dilatancy zones increases with the cycling amplitude. It is interesting that as long as the cycling amplitude is kept constant, the cycling rate does not have a significant impact on the dilatancy zones. It is worth noting that the sizes of all of the dilatancy zones are fairly small and never exceed 70 % of the cavern radius. Although they appear early, they do not develop far from the cavern.

The variable ζ^c_{vp} shows the part of the viscoplastic volumetric strain related to the dilatancy phenomenon (Figures 8b, 8d and 8f). For all scenarios, there is a short time during which the rock salt at the cavern wall is contracting; it then moves to a dilating behavior, and steadily dilates over time.

The tensile criterion $\lambda = 0$ corresponds to the moment at which tensile strains start to develop. Figure 9 shows the evolution of the width of the tensile zone and the history of ζ^t_{vp} at the cavern wall for all simulations. As already observed with the classical methodology, tensile zones appear later than dilatancy zones. Simulations with methane always predict

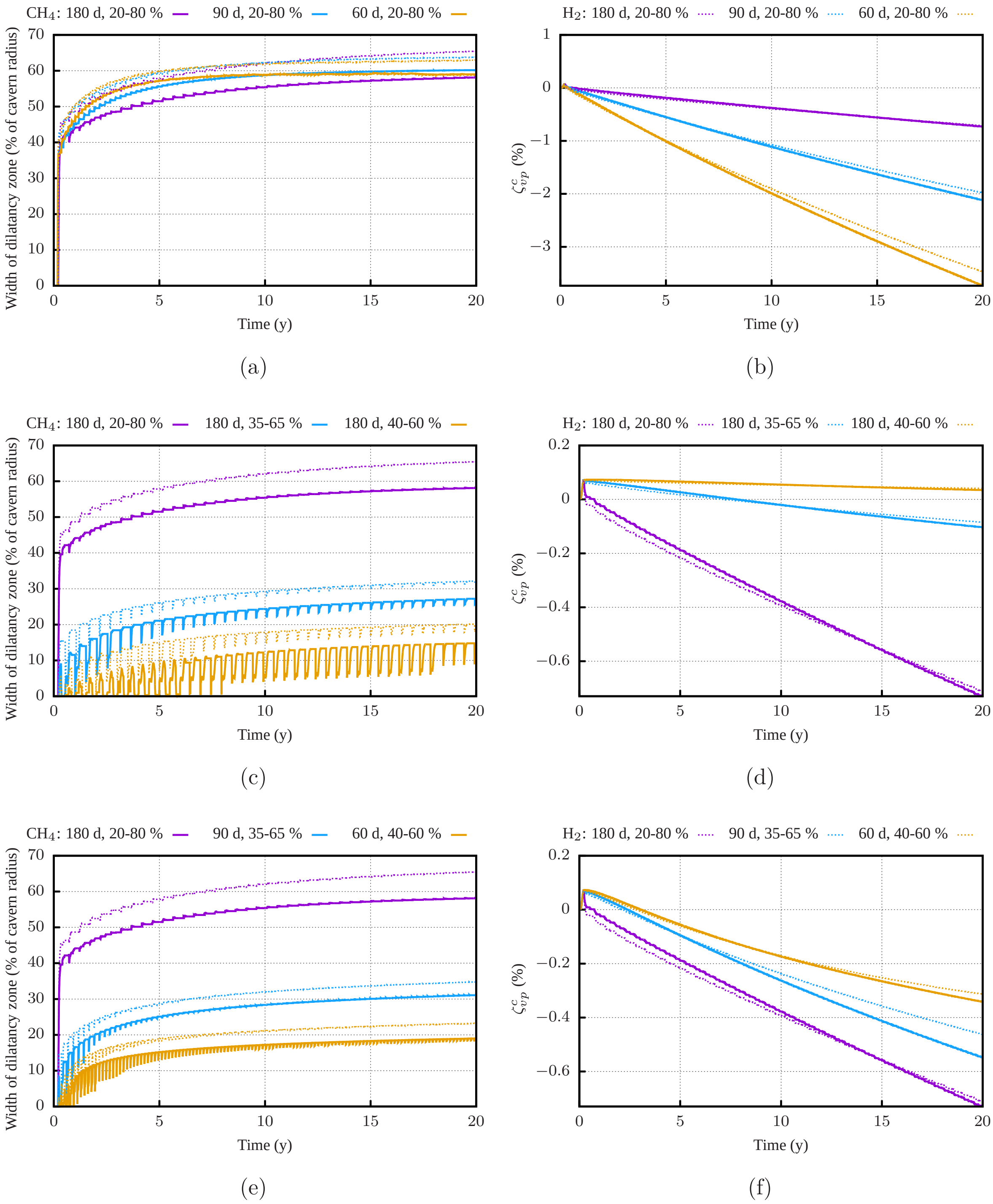

Figure 8: Evolution of the width of the dilatancy zone as a percentage of the cavern radius (left) and magnitude of the viscoplastic compressive volumetric strain at the cavern wall (right) for methane and hydrogen in all scenarios.

larger tensile zones than the ones with hydrogen, which is consistent with the classical methodology, as opposed to what was observed for dilatancy zones. This can be explained by the fact that both the old and new tensile criteria are based on the same hypothesis, which is that tension is initiated when σ_+ (which in this case corresponds to σ_1) reaches a threshold.

Figures 9a, 9c and 9e show that the tensile zones are larger not only when the cycle amplitudes are larger but also when the cycling rate is higher. The sizes of these tensile zones are very limited, less than one-tenth those of the dilatancy zones. Tensile strains only develop near the cavern.

The variable ζ_{vp}^t shows the component of the viscoplastic volumetric strain due to tension. Contrary to ζ_{vp}^c, it is always negative (always dilating), and its amplitude is much larger. Both the cycling amplitude and the loading rate significantly influence its intensity. Scenarios with large amplitudes and short cycles lead to large strains (Figure 9b). It is interesting to see that for small cycles, even though the tensile zone is smaller, the magnitude of the tensile strains can be more important (Figure 9f). As opposed to what was observed for dilatancy, the cycling rate has a direct impact on the development of tension. Moreover, although tensile zones are smaller than dilatancy zones, the damage is significantly greater.

From a thermo-mechanical point of view, the conclusions about the extent and intensity of dilatant and tensile damage are interesting in and of themselves. However, without questioning the validity of a purely thermo-mechanical analysis, dilatancy and tension may impact the hydraulic behavior of the rock salt [34, 48]. These phenomena are associated with the development of microfractures distributed in the rock mass, leading to a permeability increase and a risk of fluid permeation or leakage through the salt formation. Later, microfractures will tend to coalesce, leading to propagation of the damage zones and development of larger fractures, but that level of damage is not studied in this work.

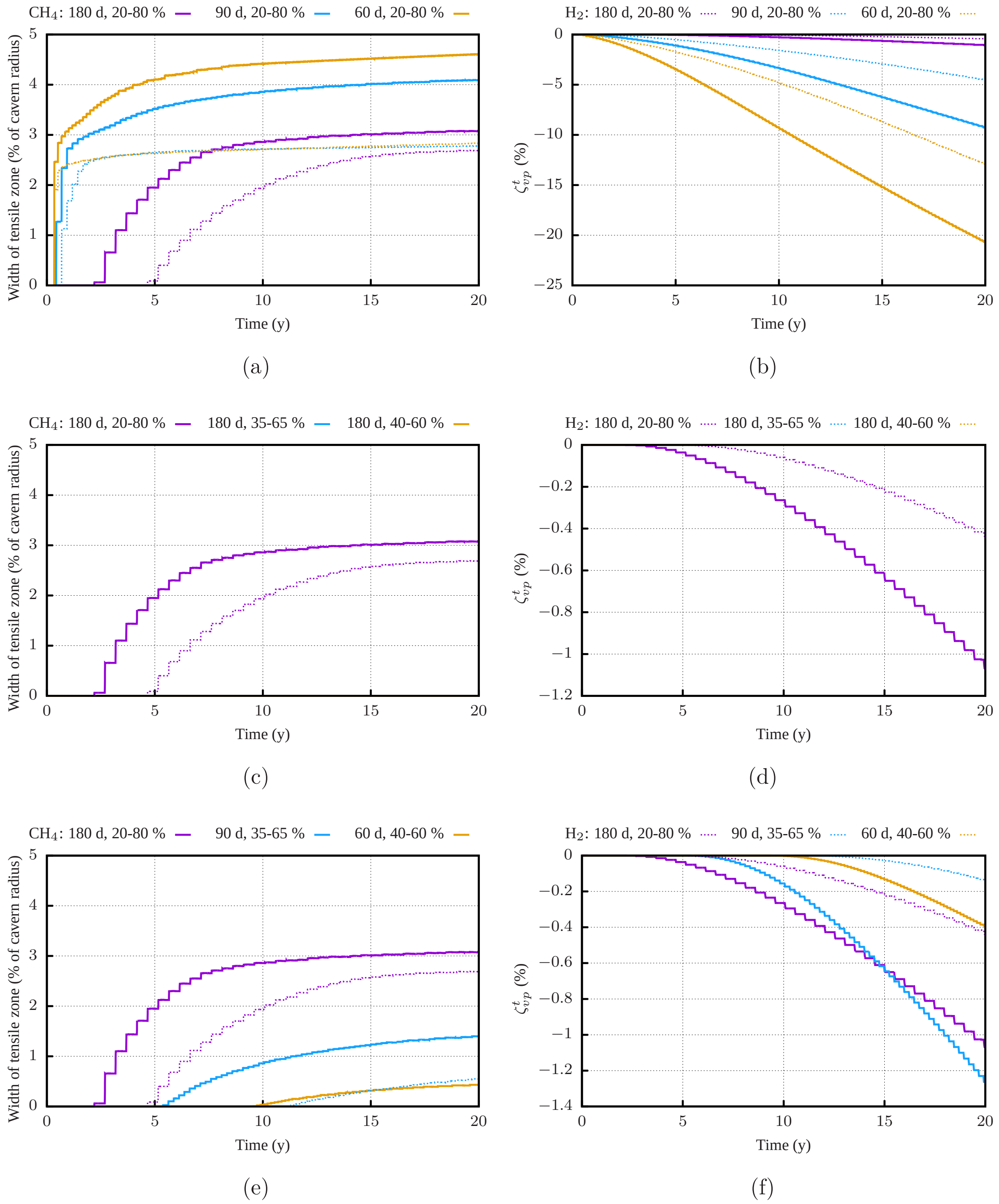

Figure 9: Evolution of the width of the tensile zone as a percentage of the cavern radius (left) and magnitude of viscoplastic tensile volumetric strain at the cavern wall (right) for methane and hydrogen in all scenarios.

5.3. Influence of dilatancy and tension on the cavern behavior

In this section, we want to assess the impact of the addition of the dilatancy and the tension phenomena in the rheological model on the cavern behavior, more precisely, on the strain at the cavern wall, and the cavern volume. We focus on the base-case scenario (180-day cycles, between 20 % and 80 % of the initial mass) for methane and compare the results of four simulations in which ($v = 0$, $\Lambda = 0$), ($v \neq 0$, $\Lambda = 0$), ($v = 0$, $\Lambda \neq 0$), and ($v \neq 0$, $\Lambda \neq 0$).

5.3.1. Strain at the cavern wall

Figure 10 shows the evolution of the viscoplastic strain at the cavern wall, for the four simulations, in terms of the viscoplastic distortion strain, $\gamma_{vp} = \sqrt{2/3}||\underline{\underline{\varepsilon}}'_{vp}||$, and viscoplastic volumetric strain $\zeta_{vp} = -\mathrm{tr}(\underline{\underline{\varepsilon}}_{vp})$. Concerning the distortion strain, the addition of the compressive volumetric strain ($v \neq 0$) has a limited impact: the difference is less than 0.2 % and the trend is not changed. The addition of the tensile component ($\Lambda \neq 0$), however, has a greater impact, almost 1 %, and the trend is modified: instead of stabilizing, the distortion strain keeps growing at a steady rate. Such an increase in the strain rate and an absence of stabilization is not encouraging from a cavern design perspective. Concerning the viscoplastic volumetric strain, it is obviously zero in the case ($v = 0$, $\Lambda = 0$). The addition of the compressive volumetric strain causes a brief contraction of the rock salt at the cavern wall, followed by a steady dilation up to 0.6 %. The addition of tension only causes a dilation, smaller at the beginning but that grows quicker and reaches 1.2 % after 20 years.

In spite of its overall increase, the time evolution of γ_{vp} exhibits cycling-induced variations due to γ^c_{vp}, itself depending on the sign of $(\sigma_r - \sigma_\theta)$. Indeed, in this case, due to the spherical geometry and 1D assumptions, the compressive component of the distortion strain γ^c_{vp} becomes $\gamma^c_{vp} = \left| \int_0^t \mathrm{sgn}(\sigma_r - \sigma_\theta)\dot{\gamma}_{vp}\mathrm{d}\tau \right|$, where $\mathrm{sgn}(\cdot)$ is the sign function. Figure 11 shows the minimum and maximum values of $(\sigma_r - \sigma_\theta)$ per cycle at the cavern wall. We can see that the value of $(\sigma_r - \sigma_\theta)$ varies between -10 and 20 MPa during each cycle, meaning that the stress state alternates between extension and compression states of stress. In addition

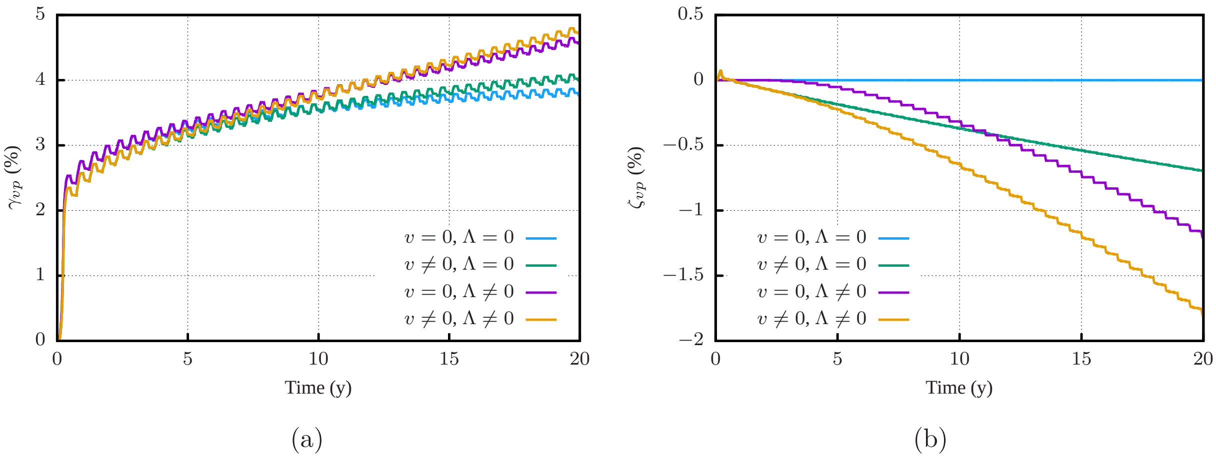

Figure 10: Viscoplastic distortion strain (a) and viscoplastic volumetric strain (b) at the cavern wall, with and without dilatancy and tension.

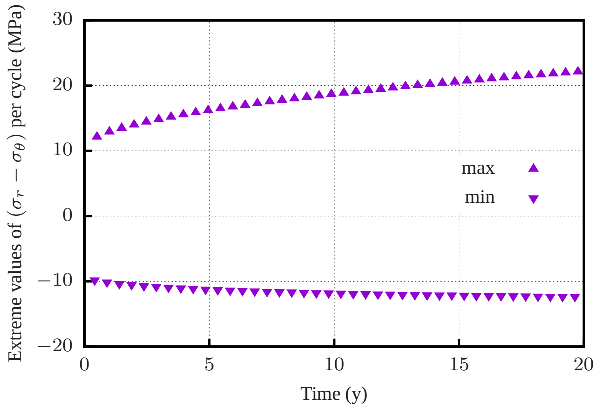

Figure 11: Minimum and maximum values of $(\sigma_r - \sigma_\theta)$ per cycle at the cavern wall.

to explaining the local variations in γ_{vp}, it fully justifies taking an interest in experimental tests alternating between compression and extension states of stress, such as [49].

It is interesting to note that, disregarding the cycling-induced variations, the shape of the curve of γ_{vp} follows the same trend as classical creep curves, without cycles, which is confirmed by Figure 12, showing the evolution of γ_{vp} in the case $(v = 0, \Lambda = 0)$, in addition to two additional simulations in which the cavern pressure is held constant at its minimum value P_{min}. For the simulations without any cycles, if the rheological parameters are left unchanged, the evolution of γ_{vp} is similar to the simulation with cycles, with a small offset.

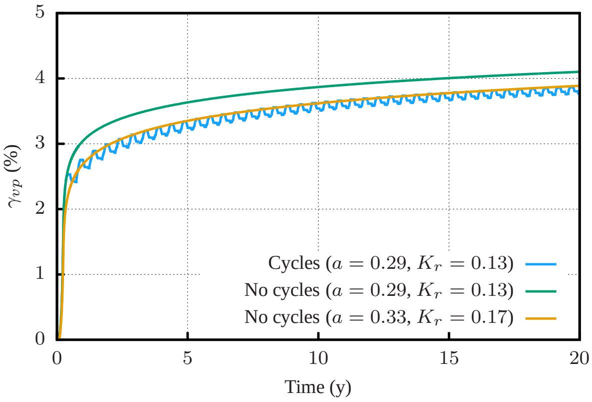

Figure 12: Viscoplastic distortion strain at the cavern wall in the case ($\upsilon = 0$, $\Lambda = 0$).

This offset can be canceled by slight variations in the rheological parameters, to within measurement and fitting error limits. In this case, P_{min} is the only element that matters for the distortion mechanism, which determinates the long-term behavior of the cavern. This result is true as long as dilatancy and tension are neglected; if they are taken into account, cycling induces complex thermo-mechanical effects and cannot be disregarded, as can be observed in Figure 10a.

5.3.2. *Cavern volume*

On the one hand, the tensile volumetric strains have a greater magnitude than the compressive volumetric strains, but on the other hand, the tensile zones are much smaller than the dilatancy zones (see Figures 8 and 9). Finally, we seek to quantify their respective influence on the cavern closure.

Figure 13 shows the evolution of the cavern volume with and without dilatancy and tension in the four cases ($\upsilon = 0$, $\Lambda = 0$), ($\upsilon \neq 0$, $\Lambda = 0$), ($\upsilon = 0$, $\Lambda \neq 0$), and ($\upsilon \neq 0$, $\Lambda \neq 0$), for methane, in the base-case scenario (180-day cycles, between 20 % and 80 % of the initial mass). Overall, the cavern volume decreases due to the creep of the surrounding rock salt, and the closing rate decreases over time. For each cycle, small variations of the cavern volume are observed, due to cycling. After 20 years, the total volume loss is approximately 5.5% and the closing rate approximately 0.015%/year. The addition of the tensile component (difference between $\Lambda = 0$ and $\Lambda \neq 0$) induces a variation of approximately 0.01% in the

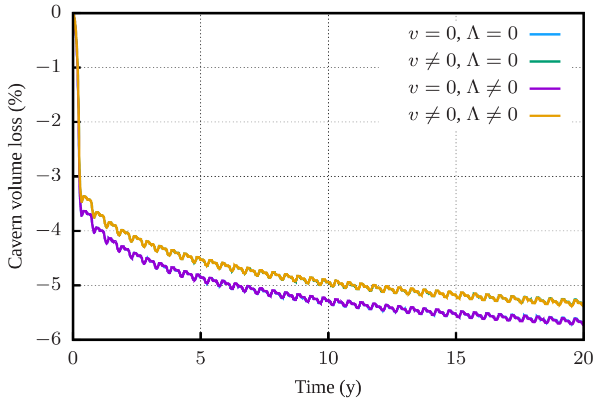

Figure 13: Evolution of the cavern volume with and without dilatancy and tension.

cavern volume loss after 20 years, and the addition of the compressive volumetric strains (difference between $v = 0$ and $v \neq 0$) causes a variation of 0.3%. These results show that dilatancy and tension have, respectively, little and no influence on the global behavior of the cavern and that the cavern volume loss is mainly due to the distortion mechanism.

To summarize these results, dilatancy and tension have no influence on the cavern pressure and temperature (Section 5.1) and a very small impact on its volume loss (this section) but significantly alter the strains at the cavern wall (Section 5.3.1). These results are interesting regarding the difficulty of the *in situ* validation of the dilatancy and tension phenomena. Indeed, with solution-mined caverns, many factors come into play (the geology around the cavern, the interactions with nearby caverns, the intricate shape of the cavern, the complex behavior of the surrounding formation material, the operating conditions, etc.), but only the global behavior of the cavern can be monitored. Pressure and temperature can possibly be directly measured with advanced techniques [50], and imaging techniques provide information about the cavern shape and size. However, local instabilities cannot be identified, and it is not possible to assess the damage of the cavern wall. Therefore, the effects of all issues listed above are blended, and telling them apart is difficult, so *in situ* validation of the dilatancy and tension phenomena is challenging. In the absence of *in situ* data, the predictive quality of any modeling approach can only be judged based on the used assumptions. In this respect, since the proposed new methodology is consistent with the rock salt

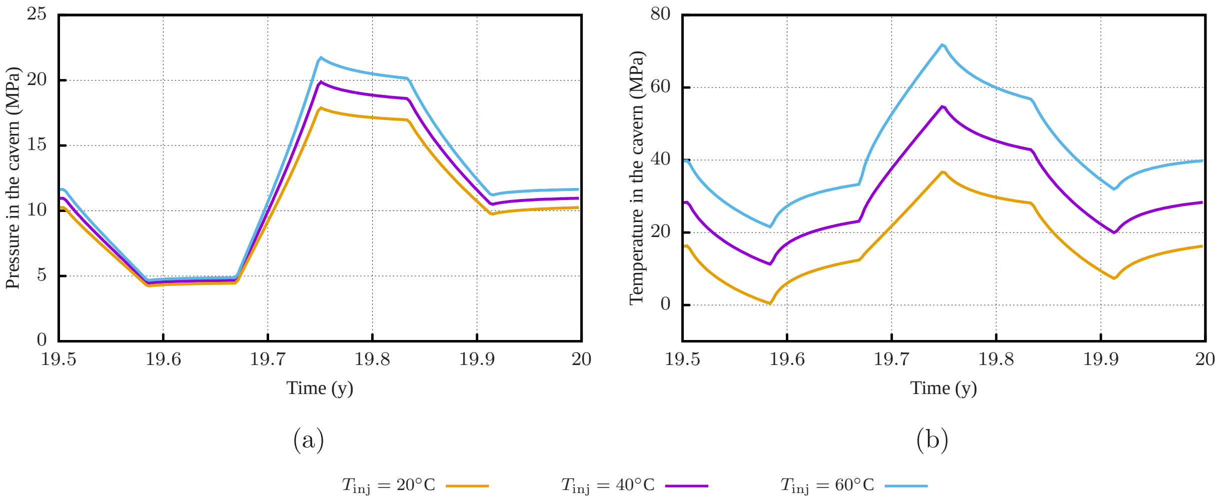

Figure 14: Evolution of the pressure (a) and temperature (b) in the cavern (last two cycles).

time-dependent behavior, unlike the classical one, it is well positioned to provide a more accurate design.

5.4. Additional results: influence of the injection temperature

One of the simplifying hypotheses that was made was to not include the well in the simulations and impose a constant injection temperature for the gas. We focus on the base-case scenario ($T_{\text{inj}} = 40$ °C), for methane, and compare it with two additional simulations identical except for the injection temperature: $T_{\text{inj}} = 20$ and 60 °C.

Figures 14a and 14b show the cavern pressure and temperature, respectively, during the last cycle for the three simulations. As the cycling amplitude is large and the mass flow is important, the injection temperature has a large influence on the cavern temperature during each filling phase. Therefore, a 20 °C difference in the injection temperature leads to a temperature difference in the cavern close to 20 °C at the end of each filling phase. It is interesting to note that this temperature difference decreases to approximately 10 °C during the gas withdrawal phase. For the highest injection temperature, the difference between the maximum and minimum temperature over the last cycle is approximately 50 °C, whereas it is less than 35 °C for the lowest injection temperature. Concerning the pressure, injection of gas with a higher temperature leads to a higher pressure in the cavern. However, the injection temperature does not have a significant impact on the minimum pressure.

Figures 15a and 15b show the evolution of the normalized width of the dilatancy and the tensile zones, respectively, for the three simulations. The injection temperature has a significant influence only on the tensile zones. High injection temperatures delay the appearance of tensile zones, but since they come with higher temperature amplitudes (see 14b) they lead to larger tensile zones.

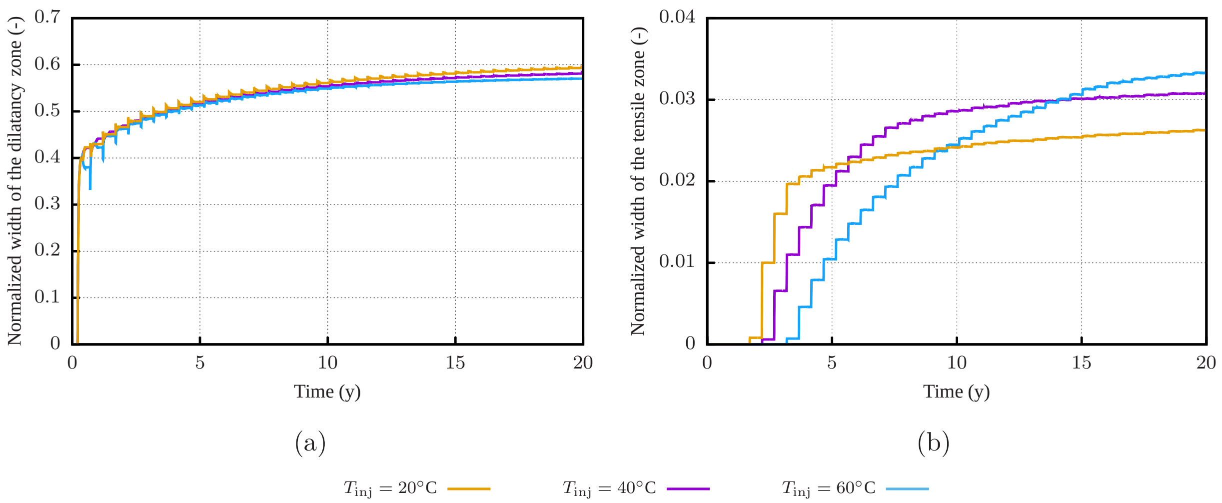

Figure 15: Evolution of the width of the dilatancy (a) and tensile (b) zones normalized with respect to the radius of the cavern for three different injection temperature.

6. Conclusions and perspectives

In this paper, we propose a new methodology to design a salt cavern that aims to reconcile the inconsistencies spotted between the creep laws and the design criteria. A new constitutive model derived from the Lemaitre creep law and including non-zero viscoplastic volumetric strains and tensile strains was developed; the model enables defining strain-based criteria. After fitting its rheological parameters simultaneously based on short- and long-term experimental tests, the new model was used in a fully coupled thermo-mechanical code to simulate salt cavern operation. The influence of different cycling scenarios and the nature of the gas stored (methane or hydrogen) were studied.

Although there is at present no field evidence or *in situ* measurement to support either the classical or the new methodology to design salt caverns, the new methodology address some of the inconsistencies within the classical methodology that have been identified. Several conclusions can be drawn:

- Dilatancy zones appear earlier and are approximately ten times larger than tensile zones. For the studied operation scenarios, the extents of all damage zones remain limited (inferior to the cavern radius).

- Shortening operation cycles while holding their amplitude constant has little influence on the dilatancy but significanly increases the tension.

- Splitting one large cycle into several small ones to *in fine* withdraw the same amount of gas allows limiting the size of the damage zones. Increasing the cycling rate, even while reducing the amplitude, leads to an increase in the magnitude of the tensile strains.

- Although methane and hydrogen exhibit contrasting thermodynamic behaviors, hydrogen storage does not raise new questions concerning the thermo-mechanical behavior of a salt cavern.

- The addition of the dilatancy and tension phenomena have little to no influence on the global behavior of the cavern.

Potential future work includes numerical developments, specifically to perform 2D and 3D simulations with the same coupling between the cavern thermodynamics and the surrounding rock salt thermo-mechanical behavior. Indeed, this paper presents fully coupled thermo-mechanical simulations in one dimension, but tensile strains may develop locally because of the intricate shapes of the caverns.

Moreover, dilatancy and tension are strongly linked to hydraulic phenomena (permeability increase, fracture development, etc.), and the storage of hydrogen leads to a higher risk of leakage than other gases (a very high diffusion coefficient because of the very small size of the molecules, low dynamic viscosity, etc.). Consequently, the hydraulic behavior should be investigated, to ultimately proceed with fully coupled thermo-hydro-mechanical simulations.

Potential future work also includes experimental and theoretical developments about cyclic loading at the constitutive level. We only study the effects of cyclic loading at the cavern scale; however elements of rock salt in the vicinity of the cavern are themselves alternatively subjected to compression and extension. Although the number of cycles is much smaller, this issue is worth studying, like the problem of fatigue in the case of steel, to validate or improve the rheological model response.

References

[1] C. Bays, Use of salt solution cavities for underground storage, in: Proceedings of the First World Salt Symposium, Cleveland, OH, 564–578, 1962.

[2] R. Thoms, R. Gehle, A brief history of salt cavern use, in: R. Geertman (Ed.), Proceedings of the 8th World Salt Symposium, The Hague, 207–214, 2000.

[3] J. Ślizowski, L. Lankof, K. Urbańczyk, K. Serbin, Potential capacity of gas storage caverns in rock salt bedded deposits in Poland, Journal of Natural Gas Science and Engineering 43 (2017) 167–178.

[4] P. V. Costa, A. M. Costa, A. Szklo, D. C. Branco, M. Freitas, L. P. Rosa, UGS in giant offshore salt caverns to substitute the actual Brazilian NG storage in LNG vessels, Journal of Natural Gas Science and Engineering 46 (2017) 451–476.

[5] S. Schiebahn, T. Grube, M. Robinius, V. Tietze, B. Kumar, D. Stolten, Power to gas: Technological overview, systems analysis and economic assessment for a case study in Germany, International journal of hydrogen energy 40 (12) (2015) 4285–4294.

[6] M. Götz, J. Lefebvre, F. Mörs, A. M. Koch, F. Graf, S. Bajohr, R. Reimert, T. Kolb, Renewable Power-to-Gas: A technological and economic review, Renewable Energy 85 (2016) 1371–1390.

[7] D. D. Peng, M. Fowler, A. Elkamel, A. Almansoori, S. B. Walker, Enabling utility-scale electrical energy storage by a power-to-gas energy hub and underground storage of hydrogen and natural gas, Journal of Natural Gas Science and Engineering 35 (2016) 1180–1199.

[8] N. Böttcher, U.-J. Görke, O. Kolditz, T. Nagel, Thermo-mechanical investigation of salt caverns for short-term hydrogen storage, Environmental Earth Sciences 76 (3) (2017) 98.

[9] M. Raju, S. K. Khaitan, Modeling and simulation of compressed air storage in caverns: a case study of the Huntorf plant, Applied Energy 89 (1) (2012) 474–481.

[10] H. Djizanne, P. Bérest, B. Brouard, The Mechanical Stability of a Salt Cavern used for Compressed Air Energy Storage (CAES), in: SMRI Spring Technical Conference, San Antonio, Texas, USA, 2014.

[11] D. E. Munson, P. R. Dawson, Salt constitutive modeling using mechanism maps, in: First Conference on the Mechanical Behavior of Salt, Pennsylvania State University, 717–737, 1981.

[12] M. Tijani, G. Vouille, B. Hugout, Le sel gemme en tant que liquide visqueux, in: Congrès International de Mécanique des Roches, Melbourne, 241–246, 1983.

[13] M. Aubertin, D. E. Gill, B. Ladanyi, A unified viscoplastic model for the inelastic flow of alkali halides, Mechanics of Materials 11 (1) (1991) 63–82.

[14] N. Cristescu, A general constitutive equation for transient and stationary creep of rock salt, International Journal of Rock Mechanics and Mining Sciences & Geomechanics Abstracts 30 (2) (1993) 125–140.

[15] D. E. Munson, Extension of the M-D model for treating stress drops in salt, in: Third Conference on the Mechanical Behavior of Salt, Ecole Polytechnique, Palaiseau, France, 31–44, 1993.

[16] K. L. DeVries, K. D. Mellegard, G. D. Callahan, Salt Damage Criterion Proof-of-Concept Research, Tech. Rep. DE-FC26-00NT41026, RESPEC, Rapid City, South Dakota, 2002.

[17] S. Heusermann, O. Rolfs, U. Schmidt, Nonlinear finite-element analysis of solution mined storage caverns in rock salt using the Lubby2 constitutive model, Computers and Structures 81 (8–11) (2003) 629–638.

[18] L. Blanco-Martín, R. Wolters, J. Rutqvist, K.-H. Lux, J. T. Birkholzer, Thermal–hydraulic–mechanical modeling of a large-scale heater test to investigate rock salt and crushed salt behavior under repository conditions for heat-generating nuclear waste, Computers and Geotechnics 77 (2016) 120–133.

[19] L. L. Van Sambeek, J. L. Ratigan, F. D. Hansen, Dilatancy of rock salt in laboratory tests, International Journal of Rock Mechanics and Mining Sciences & Geomechanics Abstracts 30 (7) (1993) 735–738.

[20] C. Spiers, C. Peach, R. Brzesowsky, Long-term rheological and transport properties of dry and wet salt rocks: final report, Office for Official Publications of the European Communities, 1989.

[21] U. E. Hunsche, Failure behaviour of rock salt around underground cavities, in: Proceedings of the 7th Symposium on Salt, vol. 1, 59–65, 1993.

[22] Z. Hou, Mechanical and hydraulic behavior of rock salt in the excavation disturbed zone around underground facilities, International Journal of Rock Mechanics and Mining Sciences 40 (5) (2003) 725–738.

[23] K. DeVries, Geomechanical analyses to determine the onset of dilation around natural gas storage caverns in bedded salt, in: SMRI Spring Technical Conference, 131–150, 2006.

[24] E. Hoffman, B. Ehgartner, Using three dimensional structural simulations to study the interactions of multiple excavations in salt, International Journal of Rock Mechanics and Mining Sciences 35 (4-5) (1998) 471.

[25] S. R. Sobolik, B. L. Ehgartner, Analysis of the Stability of Large-Diameter Caverns for the Strategic Petroleum Reserve, in: SMRI Spring Technical Conference, Galveston, Texas, USA, 2011.

[26] C. Yang, T. Wang, H. Ma, Y. Li, X. Shi, J. Daemen, Feasibility analysis of using horizontal caverns for underground gas storage: A case study of Yunying salt district, Journal of Natural Gas Science and Engineering 36 (2016) 252–266.

[27] S. N. Moghadam, H. Mirzabozorg, A. Noorzad, Modeling time-dependent behavior of gas caverns in rock salt considering creep, dilatancy and failure, Tunnelling and Underground Space Technology 33 (2013) 171–185.

[28] S. N. Moghadam, K. Nazokkar, R. J. Chalaturnyk, H. Mirzabozorg, Parametric assessment of salt cavern performance using a creep model describing dilatancy and failure, International Journal of Rock Mechanics and Mining Sciences 79 (2015) 250–267.

[29] K. Khaledi, E. Mahmoudi, M. Datcheva, T. Schanz, Stability and serviceability of underground energy storage caverns in rock salt subjected to mechanical cyclic loading, International Journal of Rock Mechanics and Mining Sciences 86 (2016) 115–131.

[30] A. Ghasemloonia, S. Butt, Feasibility study of underground salt caverns in Western Newfoundland: experimental and finite element investigation of creep-induced damage, Journal of Mining and Environment 6 (2) (2015) 205–224.

[31] Z. Shahmorad, H. Salarirad, H. Molladavoudi, A study on the effect of utilizing different constitutive models in the stability analysis of an underground gas storage within a salt structure, Journal of Natural Gas Science and Engineering 33 (2016) 808–820.

[32] T. Wang, C. Yang, H. Ma, Y. Li, X. Shi, J. Li, J. Daemen, Safety evaluation of salt cavern gas storage close to an old cavern, International Journal of Rock Mechanics and Mining Sciences 83 (2016) 95–106.

[33] R. Wolters, Thermisch-hydraulisch-mechanisch gekoppelte Analysen zum Tragverhalten von Kavernen im Salinargebirge vor dem Hintergrund der Energieträgerspeicherung und der Abfallentsorgung, Ph.D. Dissertation, Technischen Universität Clausthal, 2014.

[34] J. Stormont, J. Daemen, C. Desai, Prediction of dilation and permeability changes in rock salt, International journal for numerical and analytical methods in geomechanics 16 (8) (1992) 545–569.

[35] B. Brouard, P. Bérest, M. Karimi-Jafari, Onset of tensile effective stresses in gas storage caverns., in: SMRI Fall Technical Conference, 119–135, 2007.

[36] P. Sicsic, P. Bérest, Thermal cracking following a blowout in a gas-storage cavern, International Journal of Rock Mechanics and Mining Sciences 71 (2014) 320–329.

[37] P. Labaune, A. Rouabhi, M. Tijani, L. Blanco-Martín, T. You, Dilatancy Criteria for Salt Cavern Design: A Comparison Between Stress-and Strain-Based Approaches, Rock Mechanics and Rock Engineering (2017) 1–13.

[38] D. Bigoni, A. Piccolroaz, Yield criteria for quasibrittle and frictional materials, International Journal of Solids and Structures 41 (11) (2004) 2855–2878.

[39] I. Carol, E. Rizzi, K. Willam, On the formulation of anisotropic elastic degradation.: II. Generalized pseudo-Rankine model for tensile damage, International Journal of Solids and Structures 38 (4) (2001) 519–546.

[40] J. Chaboche, P. Lesne, J. Maire, .-C. F. Office National d'Etudes et de Recherches Aerospatiales (ONERA), Phenomenological damage mechanics of brittle materials with description of unilateral damage effects, Fracture and Damage in Quasibrittle Structures (1994) 75–84.

[41] A. Rouabhi, G. Hévin, A. Soubeyran, P. Labaune, F. Louvet, A multiphase multicomponent modeling approach of underground salt cavern storage, Geomechanics for Energy and the Environment 12 (2017) 21–35.

[42] A. Ozarslan, Large-scale hydrogen energy storage in salt caverns, International Journal of Hydrogen Energy 37 (19) (2012) 14265–14277.

[43] A. Le Duigou, A.-G. Bader, J.-C. Lanoix, L. Nadau, Relevance and costs of large scale underground hydrogen storage in France, International Journal of Hydrogen Energy 42 (36) (2017) 22987–23003.

[44] J. Michalski, U. Bünger, F. Crotogino, S. Donadei, G.-S. Schneider, T. Pregger, K.-K. Cao, D. Heide, Hydrogen generation by electrolysis and storage in salt caverns: Potentials, economics and systems aspects with regard to the German energy transition, International Journal of Hydrogen Energy 42 (19) (2017) 13427–13443.

[45] V. Tietze, D. Stolten, Comparison of hydrogen and methane storage by means of a thermodynamic analysis, International Journal of Hydrogen Energy 40 (35) (2015) 11530–11537.

[46] U. Setzmann, W. Wagner, A new equation of state and tables of thermodynamic properties for methane covering the range from the melting line to 625 K at pressures up to 100 MPa, Journal of Physical and Chemical reference data 20 (6) (1991) 1061–1155.

[47] O. Kunz, W. Wagner, The GERG-2008 wide-range equation of state for natural gases and other mixtures: an expansion of GERG-2004, Journal of chemical & engineering data 57 (11) (2012) 3032–3091.

[48] W. Liu, N. Muhammad, J. Chen, C. Spiers, C. Peach, J. Deyi, Y. Li, Investigation on the permeability characteristics of bedded salt rocks and the tightness of natural gas caverns in such formations, Journal of Natural Gas Science and Engineering 35 (2016) 468–482.

[49] L. A. Roberts, S. A. Buchholz, K. D. Mellegard, U. Düsterloh, Cyclic loading effects on the creep and dilation of salt rock, Rock Mechanics and Rock Engineering 48 (6) (2015) 2581–2590.

[50] M. Klafki, T. Wagler, S. Grosswig, A. Kneer, Long-term downhole fibre optic temperature measurements and CFD-modeling for investigation of different gas cavern operating modes., in: SMRI Fall Technical Conference, 2003.